Geol. Mag. **149** (*4*), *2012, pp. 606–625. © Cambridge University Press 2011*
doi:10.1017/S0016756811000884

Cambrian to early Silurian ophiolite and accretionary processes in the Beishan collage, NW China: implications for the architecture of the Southern Altaids

S. J. AO*†, W. J. XIAO*, C. M. HAN*, X. H. LI*, J. F. QU‡, J. E. ZHANG*, Q. Q. GUO* & Z. H. TIAN*

*State Key Laboratory of Lithospheric Evolution, Institute of Geology and Geophysics, Chinese Academy of Sciences, Beijing 100029, China
‡Institute of Geology, Chinese Academy of Geological Sciences, Beijing 100037, China

(*Received* 17 February 2011; *accepted* 20 May 2011; *first published online* 20 October 2011)

Abstract – The mechanism of continental growth of the Altaids is currently under debate between models invoking continuous subduction-accretion or punctuated accretion by closure of multiple ocean basins. We use the Yueyashan–Xichangjing ophiolite belt of the Beishan collage (southern Altaids) to constrain the earliest oceanic crust in the southern Palaeo-Asian Ocean. Five lithotectonic units were identified from S to N: the Huaniushan block, a sedimentary passive margin, the structurally incoherent Yueyashan–Xichangjing ophiolite complex, a coherent sedimentary package and the Mazongshan island arc with granitic rocks. We present a structural analysis of the accretionary complex, which is composed of the incoherent ophiolitic melange and coherent sedimentary rocks, to work out the tectonic polarity. A new weighted mean ^{206}Pb–^{238}U age of 533 ± 1.7 Ma from a plagiogranite in the Yueyashan–Xichangjing ophiolite indicates that the ocean floor formed in early Cambrian time. Furthermore, we present new geochemical data to constrain the tectonic setting of the Yueyashan–Xichangjing ophiolite. The Yueyashan–Xichangjing ophiolite was emplaced as a result of northward subduction of an oceanic plate beneath the Mazongshan island arc to the north in late Ordovician to early Silurian time. Together with data from the literature, our work demonstrates that multiple overlapping periods of accretion existed in the Palaeozoic in the northern and southern Altaids. Therefore, a model of multiple accretion by closure of several ocean basins is most viable.

Keywords: Beishan, Yueyashan–Xichangjing, ophiolite, accretionary complex, Altaids.

1. Introduction

The Altaids (Şengör, Natal'in & Burtman, 1993; Şengör & Natal'in, 1996; Xiao *et al*. 2004*a,b*) or the Central Asian Orogenic Belt (CAOB) (Carroll *et al*. 1990; Carroll *et al*. 1995; Jahn, Wu & Chen, 2000*a,b*; Dobretsov, Buslov & Vernikovsky, 2003), one of the world's largest accretionary orogens, is a collage of continental fragments, island arcs, oceanic plateaux, arc-related volcanic and granitic rocks, accretionary complexes and dismembered ophiolites (Şengör, Natal'in & Burtman, 1993; Şengör & Natal'in 1996; Jahn *et al*. 2004; Xiao *et al*. 2004*a,b*, 2010*a*; Cawood *et al*. 2009). However, the architecture of the Altaids is hotly debated. Some researchers have proposed one long-lived, single subduction system (Şengör, Natal'in & Burtman, 1993; Şengör & Natal'in, 1996; Bazhenov *et al*. 2003; Collins *et al*. 2003; Abrajevitch *et al*. 2007; Levashova *et al*. 2007), whereas others envisage punctuated accretion and closure of multiple ocean basins now marked by ophiolitic sutures (Coleman, 1989; Buchan *et al*. 2001). To resolve this architectural controversy, it is crucial to find a means of deciding whether there were multiple subduction zones in the Palaeo-Asian Ocean or just one continuous subduction zone that generally migrated southwards (present coordinates).

Although it is generally accepted that the accretionary process of the Altaids migrated southwards (Şengör, Natal'in & Burtman, 1993; Şengör & Natal'in, 1996; Windley *et al*. 2007), only the earliest subduction event in the northern Altaids has been constrained by a *c*. 1.0 Ga supra-subduction-zone (SSZ) type ophiolite (Khain *et al*. 2002), but it is not well understood when subduction started in the southern Altaids. In order to resolve this problem, it is necessary to constrain the age of the earliest subduction in the southern Altaids, and thus better understand the processes of continental growth. Accordingly, the age and tectonic relationships of key ophiolites in the southern Altaids provide the most viable key for resolving the major controversy regarding the architecture of the Altaids.

The Beishan collage in northwestern China contains some of the best ophiolites of possible early Palaeozoic age in the southern Altaids (Fig. 1). In a companion paper, Mao *et al*. (2011) describe the implications of the Liuyan Complex ophiolite in the evolution of the Altaids. In this paper we present the results of a detailed structural, geochemical and geochronological study of the Yueyashan–Xichangjing ophiolite, one of the best exposed and preserved Beishan ophiolites. We put the tectonic setting of this dated ophiolite and associated

†Author for correspondence: asj@mail.iggcas.ac.cn

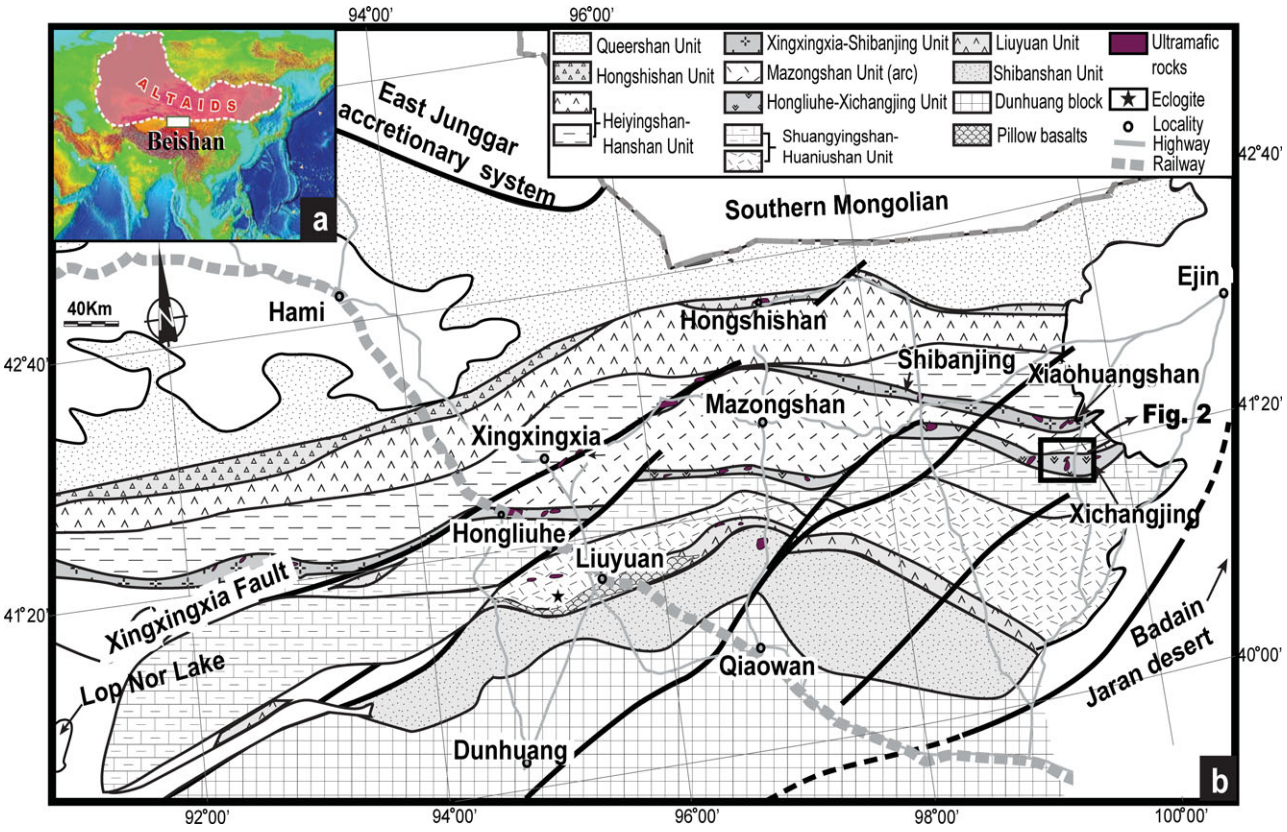

Figure 1. (Colour online) (a) Shows the location of the Beishan area in the Altaids. (b) Schematic geological map of the Beishan collage (modified after Xiao *et al*. 2010*b*). Box shows location of the larger scale map of Figure 2.

accretionary complex into a regional tectonic framework in order to demonstrate the accretionary tectonics between a micro-continental block and an island arc.

2. Regional geology and tectonic framework

2.a. Regional geology

The Beishan is an E–W-trending mountain chain in Xinjiang and Gansu provinces of NW China, situated between the Badain Jaran desert to the east and Lop Nor Lake to the west, and between Mongolia to the north and the Dunhuang to the south (Fig. 1). Across the Mongolian–Chinese border, the Beishan can be tectonically correlated with southern Mongolia, which is part of the southern Mongolian accretionary collage (Fig. 1). The southernmost unit of the Beishan collage is the Dunhuang Block. Rocks in the Beishan area were originally mapped as Precambrian to late Palaeozoic, occurring in supposedly fault-bound blocks (Zuo *et al*. 1991; Hsu *et al*. 1992; Liu & Wang, 1995). The Beishan area is not only characterized by many mafic-ultramafic complexes, which host magmatic Cu–Ni sulphide deposits that crop out along regional large-scale faults or sutures (Mao *et al*. 2008; Pirajno *et al*. 2008; Zhang *et al*. 2008; Ao *et al*. 2010), but also by four different ophiolite belts that from north to south are: Hongshishan, Shanbanjing–Xiaohuangshan, Yueyashan–Xichangjing and Liuyuan (Huang & Jin, 2006; Song *et al*. 2008; Xiao *et al*. 2010*b*; Zhang & Guo, 2008; Zhou, Zhao & Li, 2000).

The Yueyashan–Xichangjing ophiolite belt, situated in the middle of the Beishan area (Fig. 2), strikes NW–SE and is approximately 50 km long and up to 10 km wide (Fig. 2). Previous lithological mapping defined a complete ophiolite stratigraphy (Anonymous, 1977; Moores, 1982): i.e. ultramafic cumulates, gabbros, sheeted dykes, pillow lava and local chert and limestone (Zhou, Zhao & Li, 2000; Zuo *et al*. 1990*a*). Although the geochemistry and tectonic setting of many ophiolites are well understood (Dilek & Furnes, 2011), important questions remain regarding the inter-relationships between their internal structure, age, mechanism of emplacement and overall tectonic significance.

2.b. Tectonic framework

The rocks of the Beishan are divisible into five major lithotectonic units (Fig. 2), which from south to north are: the Huaniushan block (Unit I), a sedimented passive margin (Unit II), the incoherent Yueyashan–Xichangjing ophiolite (Unit III), a coherent sedimentary complex (Unit IV) and the Mazongshan island arc with granitic rocks (Unit V). All the lithotectonic units are juxtaposed along WNW–ESE-striking, SW-vergent thrusts (Fig. 2).

The southernmost Huaniushan block (Unit I) comprises the middle Proterozoic Dahuoluoshan

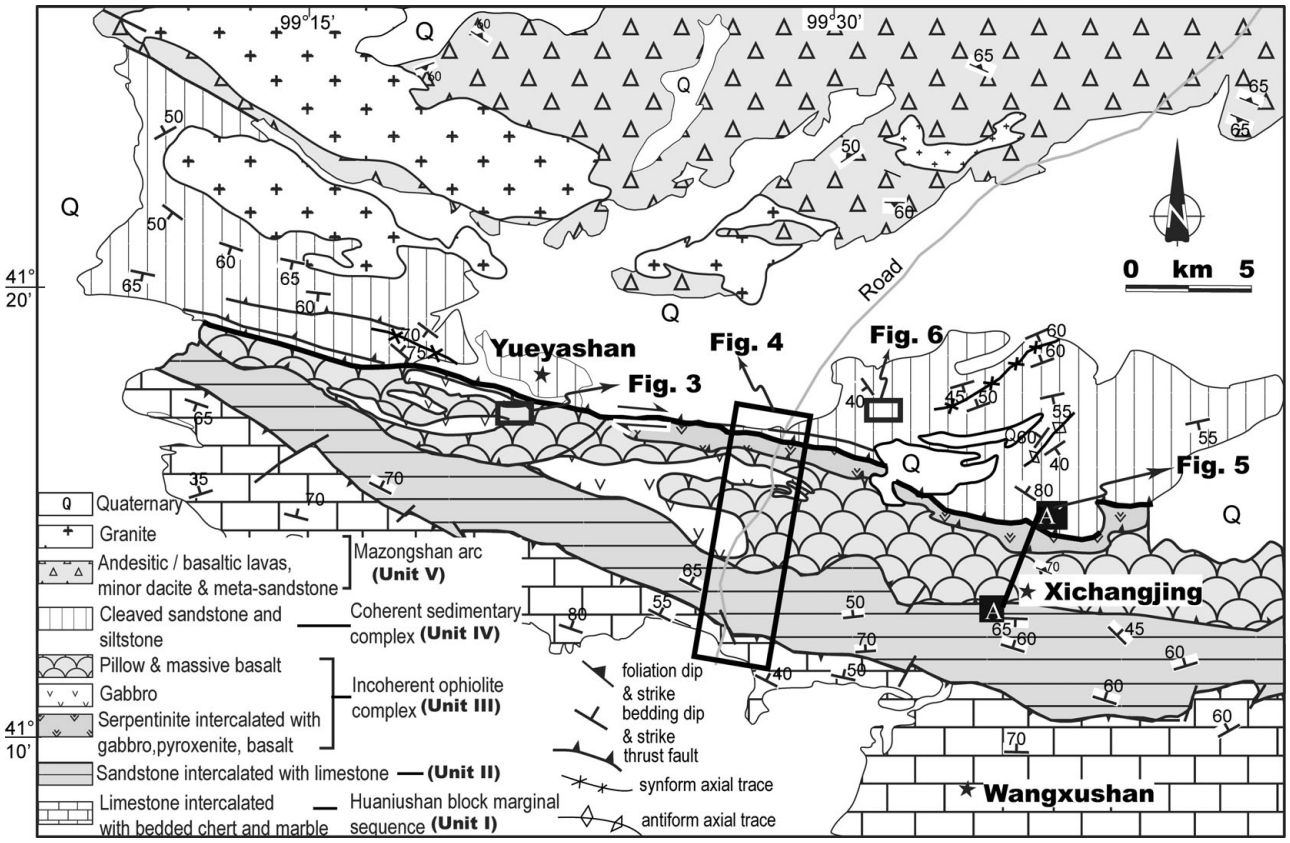

Figure 2. Geological map of the Yueyashan–Xichangjing ophiolite (modified after Anonymous, 1977, 1979). The boxes from west to east show the locations of the larger scale maps of Figures 3, 4 and 6. The section A–A′ is shown in Figure 5.

Formation, the lower part of which is mainly composed of quartzite and metasandstone with a thickness of more than 1000 m. The 4000 m thick upper Dahuoluoshan Formation consists of clastic limestone, and stromatolite-bearing limestone intercalated with beddded chert and marble. There is no precise isotopic age for this unit, and the stromatolites (*Stratifera* sp.) in the carbonates are not standard fossils with a definable lifespan (Anonymous, 1977). Based on the palaeostratigraphic assemblages this unit may be the northern limb of an anticlinorium (Figs 2, 4c), which occurs on the northern margin of a Precambrian micro-continental block.

To the north of the Huaniushan block, Unit II contains conglomerates, interbedded metasandstones, siltstones, black cherts and trilobite-bearing limestones. The well-bedded succession is dominated by sandstones and siltstones with beds about 150 m thick. The discontinuous limestone and chert beds are about 25 m thick. Palaeontological data and correlation with similar units elsewhere in Northwest China indicate these sediments have a Cambrian to early Ordovician age (Anonymous, 1977). Bedding in Unit II dips 45–65° NNE (Figs 2, 4d), but the deformation is not well developed, and consequently sedimentary graded beds are well preserved; bed-tops point NE. In most localities, Unit II lies in thrust contact with Unit I, but locally it is unconformable on Unit I. The sediments of Unit II are similar to those in a modern passive continental margin.

The Yueyashan–Xichangjing ophiolite (Unit III; Fig. 2) comprises a complete ophiolite stratigraphy: i.e. ultramafic cumulate gabbros, sheeted mafic dykes, plagiogranite dykes, pillow lavas and local cherts and limestones (Zhou, Zhao & Li, 2000; Zuo *et al*. 1990*a*). However, the ophiolite is dismembered into blocks, which have variable internal stratigraphy (Figs 3, 4, 5), and are enclosed in a matrix of sheared serpentinite.

Unit IV contains sediments (1300 m thick) that mainly comprise metasandstone interbedded with limestone and chert. Locally, contact metamorphism by intrusive granites has created quartzites and mica schists. The limestones contain brachiopods, corals and trilobites, which suggests sedimentation in late Ordovician time (Anonymous 1977, 1979). The rocks are tightly folded and cleaved, and strike WNW–ESE parallel to the regional structural trend (Figs 2, 6). The contact between these sediments and the Mazongshan island arc to the north is poorly exposed owing to low topography and Quaternary sedimentary cover, thus the contact relationship with Unit V is unclear.

Unit V, located in the northernmost part of the area, is mainly composed of andesitic to basaltic lava, together with minor dacite and metasandstone, and lenses of chert, limestone and marble. The mafic lavas belong to the Gongpoquan Formation, which consists of amygdaloidal andesite, basalt and basaltic andesite. The limestones contain abundant crinoids, bryozoans, corals and brachiopods. These corals have

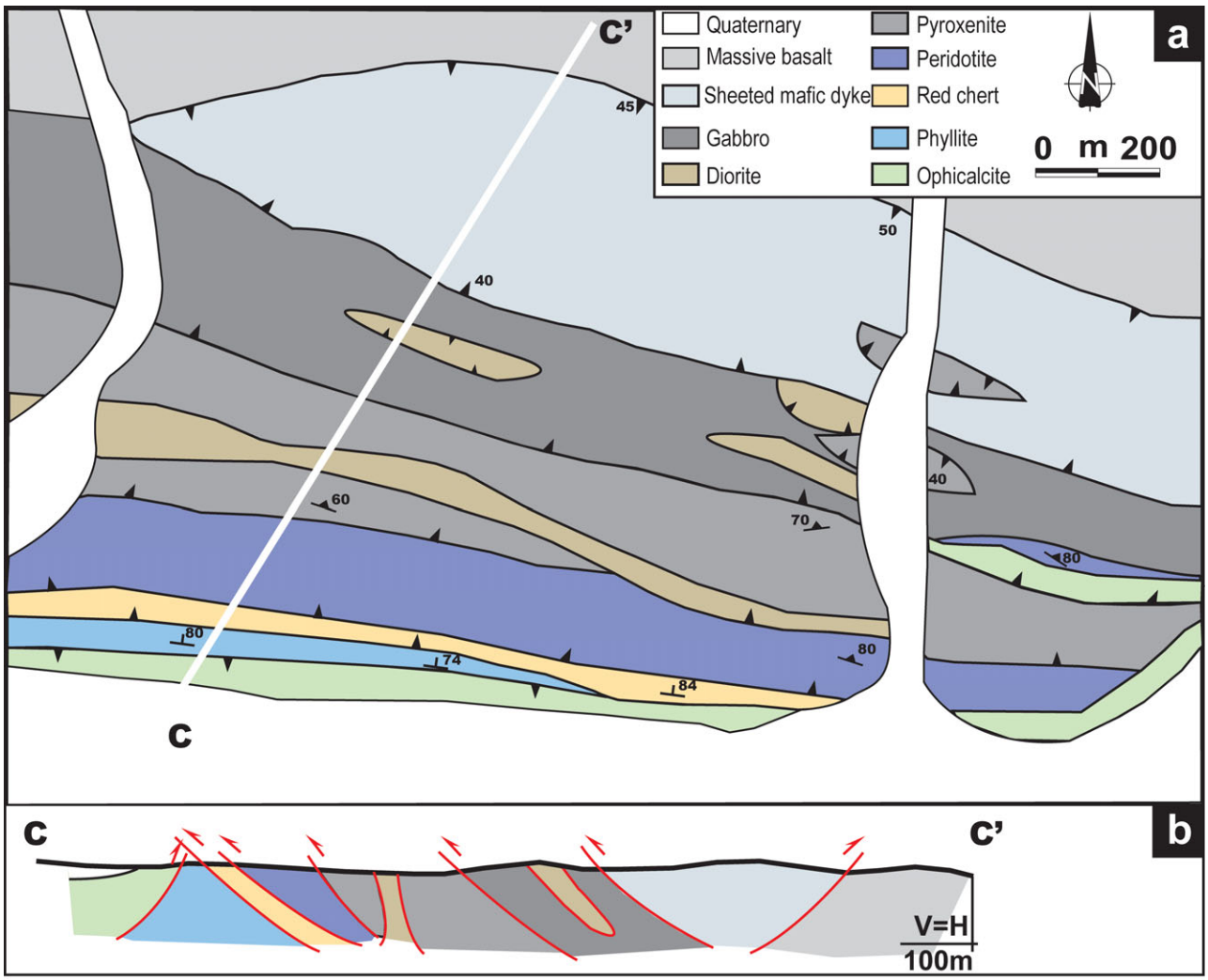

Figure 3. (Colour online) Geological map and Yueyashan cross-section of the Yueyashan–Xichangjing ophiolite (see Fig. 2 for location) (modified after Zuo *et al*. 1990*b*).

been identified as *Halysites* cf. *vulgaris kasachstanica* Polotavzeva of middle Silurian age (Anonymous, 1977). The lithological assemblages of Unit V suggest that it formed in an island arc setting (Liu & Wang, 1995; Zuo, Liu & Liu, 2003). Unit V was intruded by granitic bodies, which are mainly tonalite with minor biotite granite; a calc-alkaline signature indicates that they possibly formed in an arc-related setting (Zuo *et al*. 1990*a,b*; Liu & Wang 1995; Zuo, Liu & Liu, 2003).

The ophiolite and associated rocks in Units III and IV are the main focus of the current study, which includes a structural analyses of the two units.

3. Structural analysis

Three cross-sections of the incoherent ophiolite complex are presented (Unit III, Fig. 2) and one outcrop-scale mapping of the coherent sedimentary complex (Unit IV). These sections are mainly based on our own field work combined with previous work (Hsu *et al*. 1992; Zuo *et al*. 1990*b*). In the following paragraphs, we describe the major structural and geological features along these sections that can be considered representatives of the study region because of their location.

3.a. Ophiolitic melange

3.a.1. Yueyashan section

The Yueyashan section located in the west of the Yueyashan–Xichangjing ophiolite belt contains all the stratigraphic components of a typical ophiolite, including peridotite, gabbro, diorite, serpentinite, sheeted mafic dykes and submarine pillow lava (Fig. 3). In stratigraphic contact above the pillow lavas are Ordovician phyllites, slates, radiolarian cherts and limestones (Zuo *et al*. 1990*a*; Hs*u et al*. 1992). The ophiolitic rocks, metamorphosed in part, occur as isolated blocks or fragments in a pelitic matrix (Fig. 3a). The boundaries between the different blocks are thrusts according to Zuo *et al*. (1990*a*), as shown in Figure 3b.

3.a.2. Jiuquan–Ejinaqi road section

All the Units I, II, III and IV crop out along a dirt road in this section (Fig. 4). Bedding in Units I and II dips 45–65° N–NE (Fig. 4c,d). Unit I occurs in the

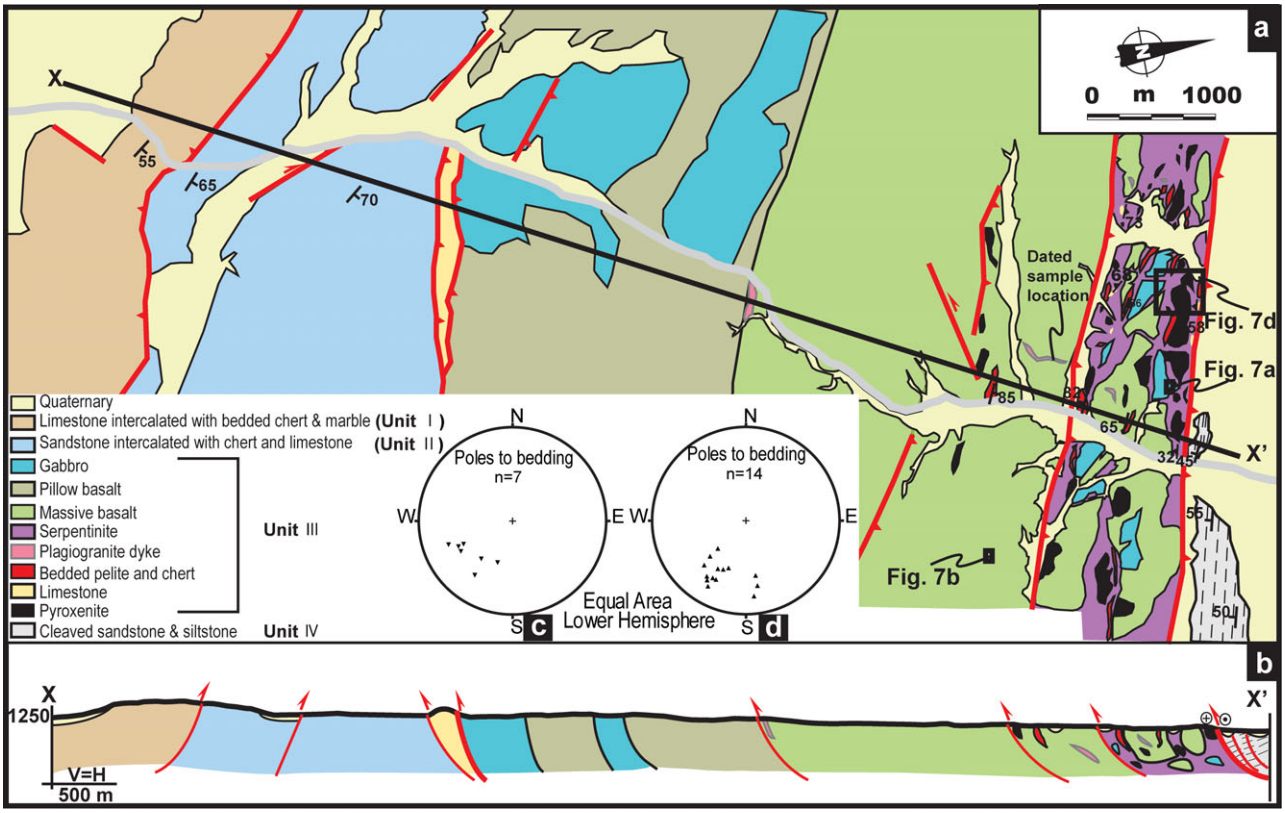

Figure 4. (Colour online) (a, b) Geological map and the Jiuquan–Ejinaqi road cross-section of the Yueyashan–Xichangjing ophiolite (see Fig. 2 for location). (c) Bedding measurements in Unit I along the dirt road section. Equal-area projection of the lower hemisphere. (d) Bedding measurements in Unit II along the dirt road section. Equal-area projection of the lower hemisphere.

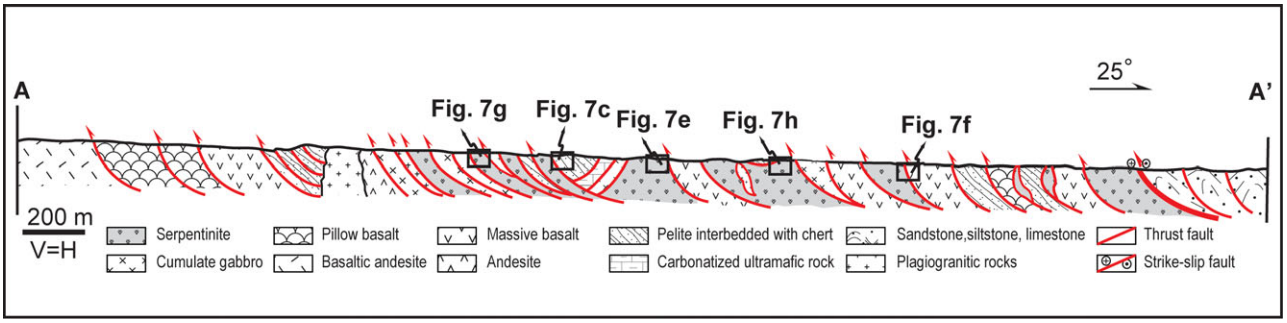

Figure 5. (Colour online) The Xichangjing cross-section of the Yueyashan–Xichangjing ophiolite (see Fig. 2 for location). The boxes show the locations of photographs in Figure 7.

northern limb of an anticlinorium that occurs on the northern margin of a Precambrian micro-continental block (Anonymous, 1977). The deformation in Unit II is not well developed, and consequently sedimentary graded beds are well preserved; bed-tops point NE. Unit II lies in thrust contact with Unit I, but locally it is unconformable on Unit I (Fig. 4b).

The Yueyashan–Xichangjing ophiolite (Unit III; Fig. 4) contains many large blocks and some almost complete sections of ophiolite stratigraphy. The blocks include ultramafic cumulates, gabbros, sheeted mafic dykes, plagiogranite dykes, pillow lavas and locally chert and limestone, which are situated in a matrix of sheared serpentinite (Fig. 4a,b). Most of the large blocks are composed of cumulate-layered gabbro, but the variable dip directions of the layering suggest they are isolated and separate blocks within the serpentinite melange (Fig. 7). The southern part of Unit III is dominated by basalt and gabbro in contrast to the northern part. The boundaries between the four units are NE-dipping thrusts, which demonstrate a top-to-the-SW sense of movement (Fig. 4b).

The northernmost part of this section exposes an imbricate thrust stack belonging to Unit IV (Fig. 4a,b). The bedded sandstones and siltstones dip moderately to the SW. The rocks are stacked by imbricate faults that dip to the NE–N and demonstrate a top-to-the-SW–S movement. The contact between Unit IV and Unit III to the south is probably a transpressional fault. Thin-sections of mylonitized gabbro close to this fault demonstrate sinistral shear or a top-to-the-E movement (Fig. 8).

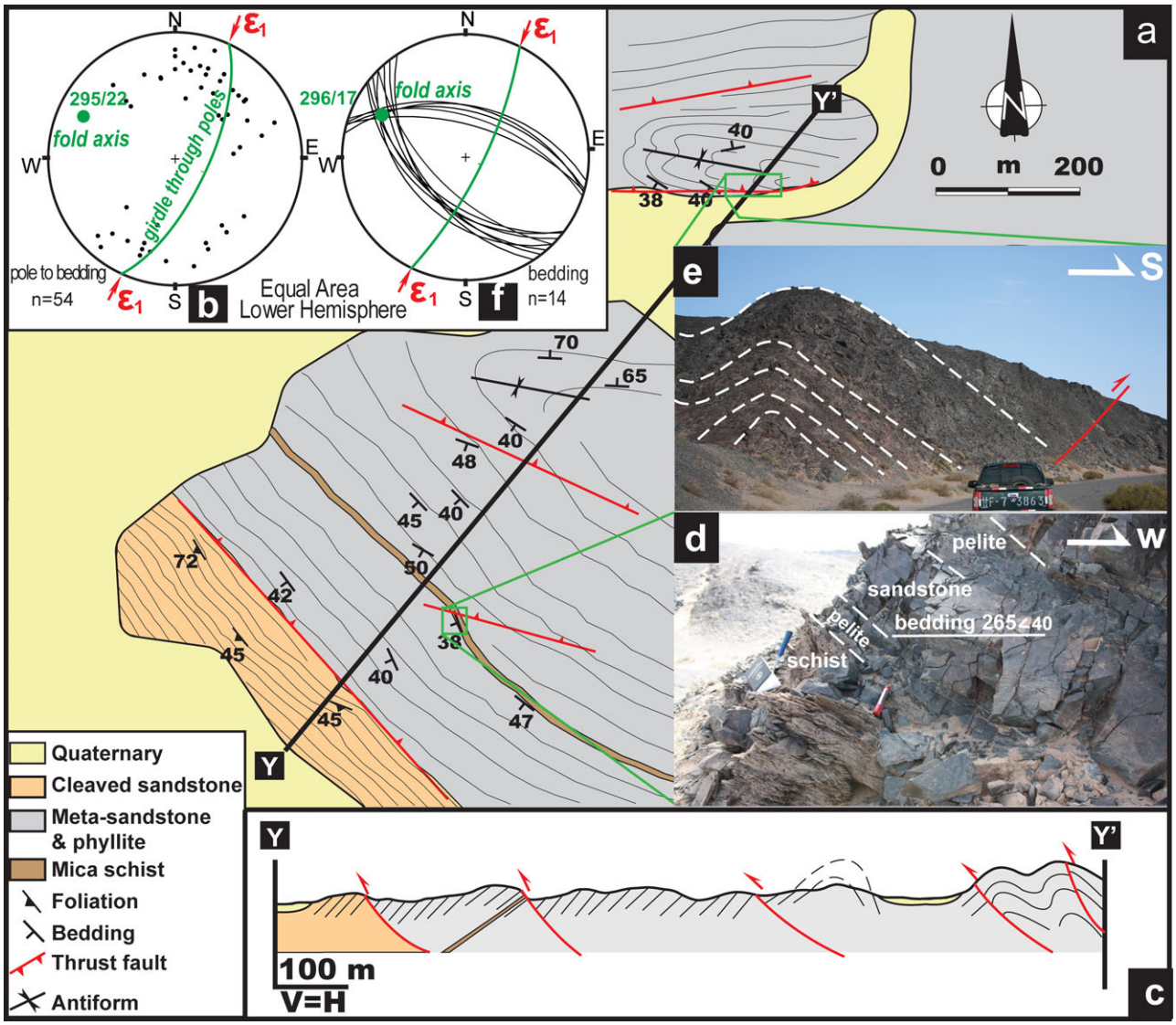

Figure 6. (Colour online) (a, c) The map and cross-section of the coherent sedimentary complex. Bedding orientations indicated on Figure 2 (Anonymous, 1977, 1979) are plotted in (b). Our own observations measured in Unit IV (a, f) are in line with published measurements, and indicate a NE–SW contraction direction that gave rise to the folding. (e) Bedded metasandstones and phyllites are folded with amplitudes of tens of metres. Car for scale; looking east. (d) Outcrop of the coherent sedimentary complex. Red pen for scale; looking south.

3.a.3. Xichangjing section

In the east of the Yueyashan–Xichangjing ophiolite belt is the Xichangjing section (Fig. 2); isolated blocks occur in a pelitic or serpentinite matrix along a N–S-striking dry creek (Figs 5, 7e,f). Lithologically the blocks consist of carbonatized peridotite, pyroxenite, gabbro, basalt and red chert. The boundaries between blocks are mostly ENE-dipping thrusts that demonstrate a top-to-the-SSW sense of movement. This imbricated thrust stack includes gabbro, serpentinite, chert and pyroxenite (Fig. 7g,h).

3.b. Coherent sedimentary rocks

The thrust rocks of Unit IV are dominated by metasandstone and mica schist (Fig. 6), which are different from those of Unit II, suggesting that the two units formed in different environments. The rocks of Unit IV are folded into a near E–W-trending, W-plunging anticline, and they are more strongly deformed than those of Unit II.

The geological map (Fig. 2) of Unit IV (Anonymous, 1977) shows the attitude of bedding data, which when plotted give an average fold axis that plunges 22° to 295° (Fig. 6b). Even though on a large scale Unit IV has the form of an anticline, its internal structure is dominated by thrusts, as indicated on the map (Fig. 6a,c). In the northern part of the map, bedded metasandstone and phyllite are deformed into folds with amplitudes of tens of metres (Fig. 6e); a plot of their bedding planes indicates a fold axis that plunges 17° to 296° (Fig. 6f), which is close to that constructed from bedding data on the geological map. The fold axial planes strike NW–SE and dip almost vertically.

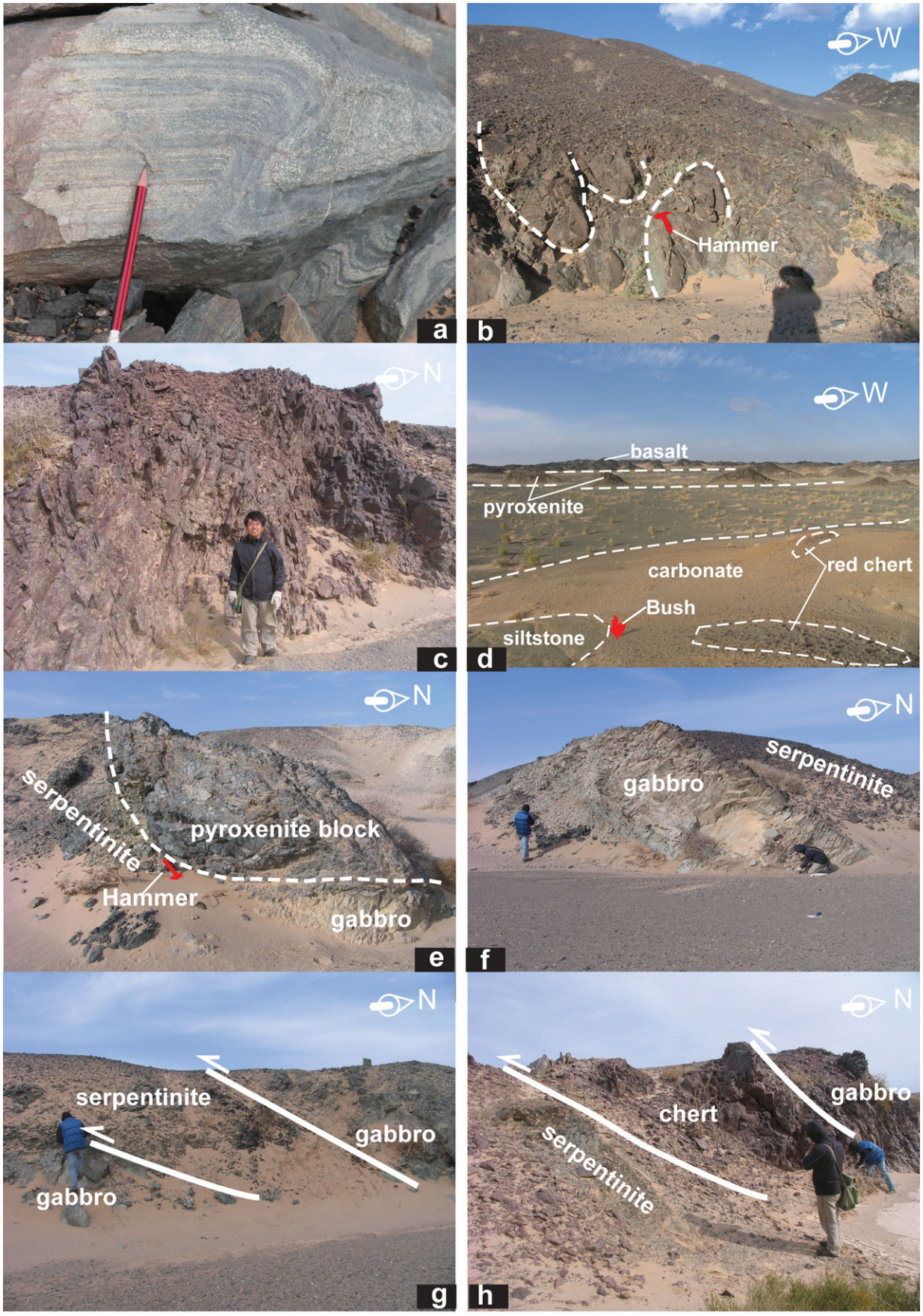

Figure 7. (Colour online) Photographs illustrating typical lithologies and structure of the Yueyashan–Xichangjing ophiolite (see Figs 4 and 5 for locations). (a) Cumulate gabbro. Pencil is 18 cm for scale. (b) Pillow basalt. Hammer for scale. (c) Red chert block in the incoherent ophiolite complex. Man for scale; looking NW. (d) Photo of the ophiolite melange in the Yueyashan area. The bush is 0.5 m high for scale; looking SW. (e) Pyroxenite block in serpentinite matrix. Hammer for scale; looking NW. (f) Gabbro blocks in serpentinite matrix. Man for scale; looking NW. (g, h) Imbricate structures in the Xichangjing area. Man for scale; looking NW.

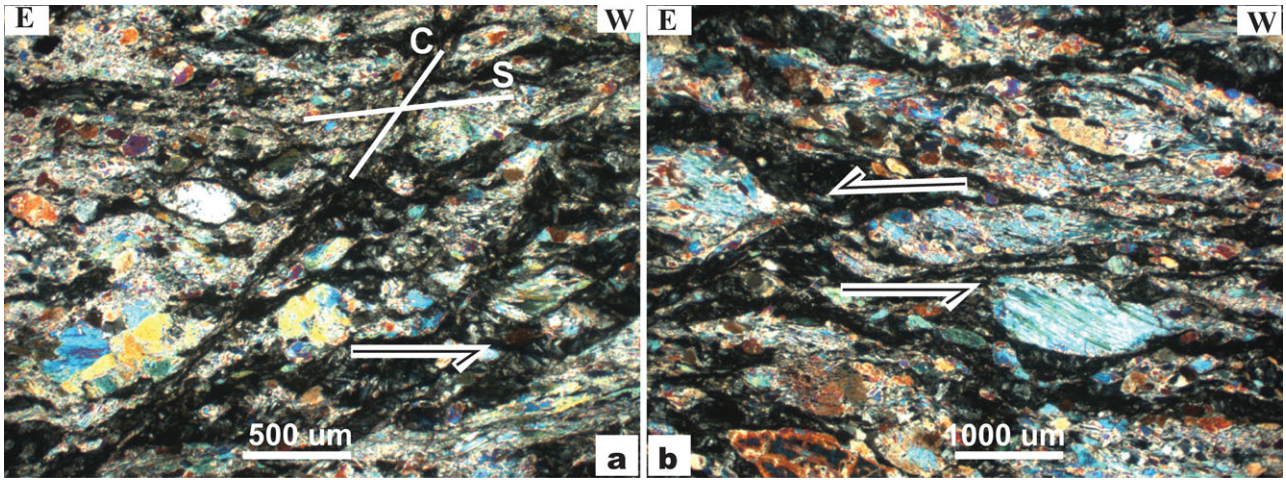

Figure 8. (Colour online) Micrographs of mylonitized gabbro showing sinistral shear sense or top-to-the-E movement. (a) The appearance of S–C fabrics under cross-polarized light. (b) Mylonitic mica-fish fabrics under cross-polarized light.

4. Geochemistry and geochronology

Whole-rock major and trace element analysis and SIMS (secondary ion mass spectrometry) U–Pb dating of zircon grains were conducted using a Cameca IMS-1280 SIMS at the Institute of Geology and Geophysics, Chinese Academy of Sciences in Beijing. The analytical procedures are described in detail in the Appendix. The geochemical and isotopic data of zircons from a plagiogranite are listed in Tables 1 and 2, respectively.

4.a. Whole-rock major and trace element analysis

Most of the analysed rocks were variably altered as indicated by the high loss on ignition (LOI) values (up to 6.15 wt % for basalt), shown in Table 1. Consequently, many major and trace elements (e.g. Si, Na, K, Ca and Cs) may have been mobilized to some extent. However, the high-field-strength elements (HFSEs), rare earth elements (REEs), some transitional elements and Th are generally immobile during hydrothermal ocean floor alteration and metamorphism and accretion-related metamorphism (Pearce, 1983). Therefore, the following discussion on petrogenesis and tectonic setting is mostly based on the HFSEs and REEs together with some transitional elements.

In order to constrain the origin and tectonic environment of the Yueyashan–Xichangjing ophiolite, refractory element contents and ratios of basalt, mafic dykes, gabbro and andesite are plotted in several chemical discrimination diagrams (Shervais, 1982; Pearce, 2008).

Basalts, gabbros and mafic dykes display a narrow range of variation for SiO_2 (38.83–54.51 wt %), MgO (3.1–8.9 wt %), low TiO_2 (0.30–1.78 wt %, Table 1) and low K_2O (0.07–1.43 wt 5%). Most of these rocks belong to the sub-alkalic series (Fig. 9a), and plot in the tholeiitic area (Fig. 9b) in a ^{T}FeO–MgO diagram (Pearce & Robinson, 2010). Overall, the basaltic rocks share low total REE (ΣREE = 12–67 ppm, Table 1), except sample 09YYS52 (ΣREE = 280.9 ppm). They display normal mid-ocean ridge basalt (N-MORB) type (La_N/Yb_N = 0.5–1.0), enriched mid-ocean ridge basalt (E-MORB) type (La_N/Yb_N = 1.0–1.3) and ocean island basalt (OIB) type (La_N/Yb_N = 28.7) REE patterns (Fig. 10b,d,f). All samples show spikes in large-ion lithophile fluid-mobile elements and negative anomalies in HFSEs (i.e. Zr, Hf, Nb, Ta; Fig. 10a,c,e). Most of them plot as N-MORB in petrogenetic-based discrimination diagrams (Pearce, 2008; Fig. 9d). Notably in Figure 9c, some data points lie above the N-MORB–OIB line and plot along a line towards the volcanic arc array. These geochemical features are indicative of an N-MORB mantle source and SSZ signature, and therefore suggest an SSZ-type ophiolite (Pearce, 2008; Pearce, Harris & Tindle, 1984; Stern & Bloomer, 1992; Stern, 2002; Pearce & Robinson, 2010).

The dated plagiogranite (Table 2) and the tonalities exhibit insignificant LREE-enriched patterns (Fig. 10h). The dated plagiogranite resembles N-MORB (Fig. 10g), but it has minor negative Nb and Ta anomalies, interpreted to be the result of residual phases in the mantle source (Brenan *et al.* 1994). Similar REE patterns suggest that the plagiogranite and tonalite originated from the same melt that generated the Yueyashan–Xichangjing ophiolite.

4.b. Geochronology of the Yueyashan–Xichangjing ophiolite

Zircon crystals separated from a plagiogranite of the Yueyashan–Xichangjing ophiolite were typically euhedral and colourless with lengths of 80–160 μm, and length/width ratios of 2:1 to 3:1. In cathodoluminescence (CL) images (Fig. 11), no inherited cores and oscillatory zones were observed. Twenty analyses, conducted on 20 zircons from the plagiogranite, show low U (64 to 342 ppm) and Th (1 to 117 ppm) concentrations as well as low Th/U ratios (0.01 to 0.34; Table 2). For geochronology, the 20 analyses

Table 1. Major oxide and trace element composition of the Yueyashan–Xichangjing ophiolite samples

Lithology	Harzburgite		Pyroxenite	Basalt	Pyroxenite	Gabbro	Layered gabbro	Mafic dyke	Basalt					Amygdaloidal basalt		
Sample no.	09YYS03	09YYS18	09YYS04	09YYS05	09YYS54	09YYS61	09YYS17-2	09YYS28	09YYS07	09YYS14	09YYS15	09YYS26	09YYS30	09YYS31	09YYS32	09YYS33
Oxides (wt %)																
SiO_2	39.55	38.05	50.55	46.85	52.59	52.23	52.44	51.06	48.24	52.61	49.67	54.51	52.52	47.03	41.27	38.38
TiO_2	0.01	0.11	0.02	1.35	0.03	0.61	0.91	1.48	0.98	0.73	0.79	0.30	0.99	0.36	0.35	0.41
Al_2O_3	0.32	2.70	0.66	14.25	0.70	14.18	14.13	13.36	14.07	15.12	15.68	21.04	13.96	12.09	10.06	10.71
$^{T}Fe_2O_3$	13.39	10.64	9.44	14.26	11.67	10.63	10.42	14.41	10.11	9.11	10.01	3.42	11.63	5.65	5.32	8.32
MnO	0.19	0.10	0.19	0.39	0.22	0.15	0.17	0.19	0.14	0.09	0.14	0.06	0.16	0.13	0.11	0.09
MgO	36.39	35.79	30.12	7.64	28.69	8.88	7.21	5.65	6.02	7.16	8.21	3.06	5.68	5.31	5.32	3.25
CaO	0.13	0.99	1.25	9.31	1.78	8.82	9.54	7.51	11.72	8.46	7.65	7.45	9.07	13.54	18.82	20.13
Na_2O	0.22	0.18	0.11	3.30	0.15	2.23	3.15	5.06	2.69	2.88	3.79	6.25	4.11	4.21	4.65	4.75
K_2O	0.01	0.02	0.01	0.08	0.01	0.81	0.60	0.28	0.35	1.16	0.51	0.25	0.12	1.43	0.27	0.11
P_2O_5	0.01	0.01	0.00	0.15	0.01	0.07	0.04	0.10	0.08	0.07	0.07	0.03	0.10	0.09	0.04	0.05
LOI	9.67	11.16	7.28	2.58	4.24	1.62	1.44	1.10	5.51	2.80	3.50	3.36	1.68	10.27	13.64	13.62
Total	99.88	99.75	99.63	100.16	100.10	100.23	100.05	100.20	99.91	100.19	100.02	99.73	100.02	100.11	99.85	99.82
Mg no.	85.69	88.11	87.54	54.13	84.41	64.79	60.38	46.34	56.74	63.39	64.37	66.34	51.83	67.43	68.78	46.25
REE (ppm)																
La	0.051	0.45	0.041	3.40	0.043	1.30	0.89	4.62	1.73	1.77	1.51	1.64	4.91	2.35	1.27	2.57
Ce	0.094	0.89	0.079	10.3	0.088	3.76	3.15	12.2	5.58	5.42	4.57	3.57	12.7	5.64	3.61	5.68
Pr	0.015	0.13	0.012	1.80	0.010	0.66	0.64	1.93	1.01	0.99	0.91	0.49	1.96	0.83	0.57	0.89
Nd	0.066	0.61	0.034	9.65	0.062	3.75	3.89	9.86	5.89	5.70	5.30	2.33	9.56	4.29	2.96	4.30
Sm	0.020	0.22	0.020	3.38	0.018	1.35	1.73	3.03	2.35	2.25	2.19	0.65	2.95	1.33	0.99	1.37
Eu	0.0067	0.088	0.0067	0.93	0.0067	0.49	0.77	1.09	0.83	0.80	0.72	0.56	0.71	0.36	0.28	0.47
Gd	0.031	0.31	0.022	4.55	0.029	1.97	2.43	3.60	3.11	3.06	3.03	0.74	3.27	1.66	1.17	1.71
Tb	0.0047	0.060	0.0035	0.85	0.0063	0.38	0.47	0.65	0.62	0.61	0.59	0.13	0.60	0.29	0.22	0.33
Dy	0.031	0.42	0.029	5.57	0.042	2.74	3.20	4.27	4.11	3.96	3.89	0.82	3.86	1.99	1.51	2.14
Ho	0.0072	0.086	0.0080	1.23	0.011	0.60	0.72	0.94	0.90	0.83	0.84	0.18	0.86	0.44	0.34	0.49
Er	0.025	0.29	0.027	3.64	0.045	1.78	2.13	2.76	2.60	2.44	2.48	0.54	2.48	1.24	1.02	1.39
Tm	0.0041	0.043	0.0043	0.54	0.0081	0.29	0.31	0.39	0.38	0.33	0.35	0.075	0.36	0.18	0.14	0.21
Yb	0.021	0.30	0.042	3.55	0.053	1.97	2.09	2.76	2.44	2.17	2.35	0.53	2.54	1.24	0.98	1.47
Lu	0.0052	0.047	0.0071	0.53	0.0100	0.30	0.31	0.38	0.36	0.33	0.33	0.079	0.35	0.18	0.14	0.21
ΣREE	0.38	3.93	0.33	49.97	0.43	21.35	22.72	48.52	31.91	30.67	29.09	12.34	47.16	22.02	15.20	23.21
Trace elements(ppm)																
Sc	9.31	16.1	21.0	40.5	27.5	42.0	43.5	39.9	39.2	38.9	41.9	8.06	41.7	28.9	26.7	31.8
V	28.3	83.0	48.5	343	59.7	295	270	512	268	224	256	81.5	380	178	164	249
Cr	3360	4443	2326	60.4	1799	213	159	80.3	356	593	598	2.29	16.1	414	518	551
Co	127	110	70.4	45.9	83.2	46.6	41.8	42.6	35.9	36.5	42.9	9.95	38.5	26.5	38.8	28.5
Ni	1014	1376	300	41.0	338	135	74.0	27.2	76.0	132	146	4.65	22.7	102	173	134
Cu	2.67	14.9	1.36	133	3.52	53.3	7.39	10.5	65.5	49.5	73.8	11.7	5.98	35.5	41.2	42.0
Zn	68.9	65.5	54.9	370	65.9	55.6	74.9	51.3	67.6	67.7	71.0	14.6	37.0	45.1	41.2	41.8
Ga	0.63	3.06	1.08	13.5	1.25	11.4	12.6	15.2	14.6	13.6	13.5	13.4	15.5	8.49	5.94	8.02
Rb	0.14	0.28	0.36	0.89	0.37	22.4	15.2	1.33	4.94	17.6	7.70	2.95	0.51	14.6	1.84	0.68
Sr	6.10	8.00	17.2	128	8.38	121	149	92.7	124	179	84.8	280	228	124	119	127
Y	0.20	2.58	0.21	34.0	0.30	16.8	19.4	25.6	24.7	22.5	23.5	5.42	23.1	12.4	8.83	13.7
Zr	0.41	3.33	0.21	65.5	0.41	23.0	25.0	51.8	54.2	37.6	38.9	15.9	50.1	19.1	17.7	21.6
Nb	0.021	0.12	0.014	3.57	0.022	1.06	0.48	1.27	0.88	0.82	0.69	0.45	1.37	0.37	0.33	0.39
Ta	0.0086	0.013	0.0074	0.20	0.0052	0.066	0.039	0.093	0.063	0.061	0.050	0.034	0.092	0.030	0.024	0.027

Lithology	Harzburgite		Pyroxenite	Basalt	Pyroxenite	Gabbro	Layered gabbro	Mafic dyke	Basalt					Amygdaloidal basalt		
Sample no.	09YYS03	09YYS18	09YYS04	09YYS05	09YYS54	09YYS61	09YYS17-2	09YYS28	09YYS07	09YYS14	09YYS15	09YYS26	09YYS30	09YYS31	09YYS32	09YYS33
Cs	0.039	0.87	0.38	0.27	0.78	2.18	1.30	0.67	0.31	0.88	0.53	0.61	0.11	0.41	0.15	0.11
Ba	14.8	13.4	8.06	18.3	8.52	50.6	73.2	38.0	70.1	77.4	54.7	44.7	27.2	180	81.4	52.3
Hf	0.014	0.12	0.0096	1.83	0.014	0.79	0.82	1.54	1.56	1.14	1.19	0.48	1.47	0.62	0.56	0.67
Pb	0.24	0.21	0.22	1.40	0.25	0.37	0.36	0.33	1.54	0.44	0.42	0.55	0.73	0.76	0.52	0.69
Th	0.012	0.044	0.020	0.094	0.0082	0.063	0.047	0.42	0.093	0.078	0.061	0.19	0.49	0.22	0.18	0.20
U	0.081	0.23	0.022	0.059	0.046	0.13	0.15	0.31	0.24	0.35	0.11	0.14	0.42	0.26	0.36	0.15

Lithology	Basalt	Mafic dyke	Dolerite	Andesite			Basalt								Gabbro	
Sample no.	09YYS34	09YYS36	09YYS38	09YYS40	09YYS41	09YYS43	09YYS44	09YYS48	09YYS52	09YYS65	09YYS73	09YYS74	09YYS60	09YYS49	09YYS51	09YYS59
Oxides (wt %)																
SiO_2	51.04	45.43	42.77	56.74	64.70	60.94	49.47	49.23	47.20	51.11	51.18	53.14	49.28	50.40	50.02	52.49
TiO_2	0.67	1.36	1.38	0.85	0.92	1.14	1.30	0.79	1.78	0.90	0.78	0.68	1.07	0.90	0.79	0.43
Al_2O_3	14.42	14.71	16.64	15.18	13.65	13.16	15.37	15.68	12.67	14.66	14.42	14.17	14.61	13.76	14.48	13.50
Fe_2O_3	8.32	17.56	15.61	10.88	8.54	10.53	14.77	9.64	9.03	12.13	10.96	10.39	11.08	9.31	11.68	9.71
MnO	0.14	0.23	0.17	0.09	0.10	0.17	0.30	0.15	0.11	0.09	0.24	0.18	0.16	0.12	0.18	0.16
MgO	6.41	6.61	6.71	3.85	1.94	2.69	5.08	8.33	8.71	5.73	6.91	7.36	6.36	5.67	8.31	8.47
CaO	8.24	7.71	11.74	4.81	2.96	3.23	5.38	9.29	9.21	8.66	7.79	5.58	11.71	10.01	8.52	9.29
Na_2O	5.47	3.46	1.76	6.10	5.79	5.19	5.33	3.30	4.07	3.48	3.98	4.61	2.55	3.51	3.44	4.23
K_2O	0.20	0.28	0.12	0.59	0.31	0.07	0.11	0.43	0.18	0.30	0.76	0.93	0.24	0.17	0.42	0.22
P_2O_5	0.07	0.15	0.03	0.08	0.25	0.22	0.15	0.07	1.48	0.09	0.08	0.10	0.09	0.07	0.13	0.03
LOI	5.11	2.48	3.26	0.86	1.02	2.14	2.87	3.30	5.32	2.74	2.90	2.34	3.04	6.15	1.80	0.92
Total	100.10	99.97	100.19	100.03	100.18	99.49	100.13	100.21	99.76	99.88	99.99	99.48	100.19	100.07	99.76	99.45
$MgO^{\#}$	62.94	45.33	48.64	43.81	33.35	36.01	43.11	65.56	68.00	51.00	58.14	60.95	55.84	57.29	61.05	65.77
REE (ppm)																
La	3.20	2.80	1.20	5.46	9.96	8.39	6.92	1.86	56.0	2.39	2.96	2.41	1.95	2.16	1.47	1.76
Ce	7.83	7.76	3.19	16.8	26.7	21.3	17.2	5.43	121	5.90	8.40	6.94	6.28	6.13	4.02	4.49
Pr	1.25	1.41	0.52	2.54	4.15	3.23	2.64	0.96	15.2	1.31	1.41	1.08	1.24	1.03	0.73	0.66
Nd	6.39	8.20	2.74	12.7	21.1	16.4	13.6	5.63	60.8	7.21	7.45	5.94	7.41	5.78	4.17	3.41
Sm	1.95	2.97	1.11	3.83	6.01	4.79	4.06	2.09	9.54	2.68	2.36	1.93	2.67	2.02	1.55	1.08
Eu	0.68	1.16	0.59	0.80	1.69	1.47	1.35	0.79	2.77	0.95	0.92	0.72	0.96	0.83	0.65	0.48
Gd	2.50	3.66	1.34	4.63	7.24	5.87	5.00	3.07	6.79	3.82	2.97	2.44	3.87	3.00	2.11	1.50
Tb	0.46	0.69	0.27	0.89	1.33	1.06	0.89	0.58	0.83	0.74	0.55	0.44	0.74	0.58	0.40	0.29
Dy	2.95	4.49	1.80	5.55	8.52	6.90	5.84	3.84	3.83	4.78	3.58	2.82	4.89	3.67	2.79	1.91
Ho	0.66	0.98	0.40	1.21	1.83	1.55	1.29	0.84	0.65	0.99	0.77	0.60	1.04	0.80	0.59	0.43
Er	1.91	2.98	1.15	3.55	5.31	4.36	3.73	2.36	1.65	2.75	2.29	1.76	2.95	2.36	1.66	1.20
Tm	0.27	0.42	0.16	0.54	0.79	0.65	0.55	0.36	0.21	0.38	0.34	0.27	0.43	0.35	0.25	0.19
Yb	1.83	2.85	1.15	3.80	5.42	4.39	3.61	2.40	1.32	2.51	2.23	1.85	2.96	2.29	1.63	1.28
Lu	0.26	0.41	0.17	0.54	0.81	0.65	0.55	0.35	0.19	0.35	0.34	0.28	0.41	0.36	0.25	0.20
ΣREE	32.14	40.79	15.79	62.85	100.86	81.03	67.30	30.55	280.92	36.76	36.56	29.49	37.78	31.35	22.27	18.88

Table 1. Continued.

Lithology	Basalt	Mafic dyke	Dolerite	Andesite			Basalt								Gabbro	
Sample no.	09YYS34	09YYS36	09YYS38	09YYS40	09YYS41	09YYS43	09YYS44	09YYS48	09YYS52	09YYS65	09YYS73	09YYS74	09YYS60	09YYS49	09YYS51	09YYS59
Trace elements (ppm)																
Sc	36.3	46.0	51.8	35.2	20.4	30.3	41.8	42.2	18.1	40.3	37.9	39.2	40.7	39.0	52.1	37.7
V	250	566	719	367	82.7	225	505	254	158	238	290	269	287	261	349	181
Cr	57.3	77.3	10.5	7.48	3.04	2.37	12.8	602	309	490	35.9	207	343	503	26.2	594
Co	32.3	52.4	42.8	16.4	16.3	26.0	46.6	38.7	38.1	27.4	35.9	36.1	35.1	34.6	54.4	45.7
Ni	30.6	37.3	34.9	22.5	1.86	1.67	9.94	147	228	149	38.8	63.5	84.1	93.5	30.9	152
Cu	240	16.1	120	7.23	61.0	58.8	14.0	76.8	45.4	24.0	3.71	7.72	59.7	88.8	200	35.7
Zn	61.3	126	92.6	28.6	50.4	51.1	178	62.0	117	71.1	58.3	55.3	77.7	59.1	63.1	64.4
Ga	11.7	18.9	19.3	13.8	16.6	14.2	17.5	14.7	18.5	14.5	13.3	12.9	15.4	13.4	15.0	10.8
Rb	1.33	3.97	1.07	5.36	2.75	0.56	2.36	6.06	2.16	3.60	7.09	8.50	3.05	2.53	6.26	0.84
Sr	133	174	205	188	162	109	111	160	673	194	159	209	163	134	141	102
Y	18.4	26.6	10.4	34.5	51.7	42.0	35.8	24.0	18.3	27.5	21.5	17.3	29.4	22.3	15.6	11.7
Zr	34.0	17.8	13.2	55.3	131	94.2	70.7	42.6	192	42.4	40.9	38.3	57.9	48.7	9.40	27.5
Nb	1.21	0.86	0.22	0.90	3.77	3.52	2.47	1.17	26.7	0.66	1.10	0.57	0.81	1.70	1.89	1.11
Ta	0.084	0.049	0.017	0.050	0.25	0.23	0.16	0.081	1.47	0.054	0.071	0.037	0.059	0.12	0.076	0.079
Cs	0.17	1.09	0.38	0.33	0.26	0.19	3.57	0.39	0.66	0.61	0.30	0.54	0.23	0.32	0.68	0.077
Ba	73.7	45.5	23.1	98.3	61.2	20.0	23.0	50.1	172	18.8	54.0	103	67.4	46.4	147	42.7
Hf	0.97	0.62	0.41	1.67	3.80	2.79	2.10	1.25	4.92	1.35	1.20	1.15	1.68	1.40	0.36	0.82
Pb	1.20	0.56	1.37	0.36	0.84	0.62	1.89	0.52	11.6	0.40	0.27	0.31	2.69	0.79	1.06	0.52
Th	0.30	0.043	0.13	0.88	1.22	0.92	0.69	0.12	5.62	0.059	0.39	0.47	0.093	0.18	0.062	0.13
U	0.25	0.24	0.33	0.51	0.80	0.53	1.03	0.068	1.42	0.13	0.18	0.15	0.14	0.39	0.19	0.15

Lithology	Basalt		Andesite	Andesite	Gabbro	Tonalite	Dacite	Dacite	Plagiogranite	Dacite	Dacite	Plagiogranite	Dacite	Dacite
Sample no.	09YYS81	09YYS84	09YYS91	09YYS92	09YYS93	09YYS01-6	09YYS27	09YYS35	09YYS39	09YYS72	09YYS45	09YYS87	09YYS82	09YYS79
Oxides (wt. %)														
SiO_2	51.19	51.58	59.27	60.51	52.57	71.38	70.27	75.13	76.82	75.82	74.30	76.59	71.35	73.55
TiO_2	1.53	1.33	1.12	1.01	0.64	0.20	0.21	0.06	0.26	0.33	0.03	0.09	0.19	0.17
Al_2O_3	14.36	14.35	13.10	12.56	13.95	15.04	14.53	13.71	11.98	11.66	14.52	13.42	14.11	14.26
Fe_2O_3	14.57	15.34	10.71	8.91	10.56	1.71	1.67	0.97	1.55	3.10	0.75	0.59	1.49	1.49
MnO	0.26	0.19	0.21	0.11	0.16	0.02	0.02	0.02	0.01	0.02	0.03	0.02	0.02	0.02
MgO	6.56	4.15	3.52	2.09	7.62	0.69	1.08	0.23	0.38	1.06	0.16	0.20	0.48	0.42
CaO	4.64	6.87	5.12	9.16	9.83	2.37	1.90	0.91	2.74	0.59	0.40	1.68	2.05	1.44
Na_2O	3.52	4.01	5.18	2.35	2.41	5.36	7.71	5.39	4.50	6.42	5.11	6.89	5.96	5.83
K_2O	0.64	0.07	0.19	0.02	0.44	1.68	0.51	2.01	0.37	0.12	3.54	0.14	1.33	1.38
P_2O_5	0.13	0.11	0.15	0.17	0.09	0.06	0.07	0.03	0.04	0.05	0.07	0.05	0.06	0.05
LOI	2.70	2.10	1.50	3.24	2.16	1.56	1.82	1.44	0.74	0.96	1.04	0.50	2.46	1.26
Total	100.11	100.09	100.07	100.14	100.43	100.07	99.79	99.90	99.39	100.13	99.95	100.18	99.50	99.87
$MgO^{\#}$	49.80	37.34	42.00	34.07	61.38	47.06	58.76	34.31	35.07	42.96	31.97	42.75	41.51	38.31
REE (ppm)														
La	6.02	5.83	4.74	6.36	3.07	9.60	14.8	15.7	3.67	8.38	7.44	2.44	9.87	13.2
Ce	15.5	15.0	11.9	16.2	8.15	18.5	28.1	31.8	7.44	22.8	18.4	4.29	19.4	23.8
Pr	2.36	2.29	1.83	2.47	1.31	2.13	3.18	3.69	0.84	3.36	2.41	0.47	2.27	2.62
Nd	12.1	11.9	9.64	12.1	6.87	8.08	11.4	13.7	3.59	16.2	9.62	1.59	8.52	9.50
Sm	3.62	3.60	3.15	4.03	2.37	1.54	1.99	2.46	0.70	4.74	3.39	0.37	1.55	1.68
Eu	1.10	1.14	1.06	1.33	0.87	0.47	0.56	0.51	0.64	1.14	0.12	0.37	0.40	0.52
Gd	4.28	4.09	4.02	4.79	3.21	1.41	1.60	1.71	0.79	5.35	3.69	0.39	1.36	1.39

Lithology	Basalt		Andesite	Andesite	Gabbro	Tonalite	Dacite	Dacite	Plagiogranite	Dacite	Dacite	Plagiogranite	Dacite	Dacite
Sample no.	09YYS81	09YYS84	09YYS91	09YYS92	09YYS93	09YYS01-6	09YYS27	09YYS35	09YYS39	09YYS72	09YYS45	09YYS87	09YYS82	09YYS79
Tb	0.77	0.74	0.74	0.88	0.61	0.19	0.21	0.24	0.14	1.03	0.69	0.087	0.19	0.19
Dy	4.92	4.66	4.72	5.66	3.94	0.94	1.04	1.20	0.90	6.77	3.94	0.60	0.92	0.92
Ho	1.01	1.02	1.07	1.23	0.86	0.16	0.20	0.21	0.22	1.48	0.74	0.15	0.16	0.17
Er	3.10	3.09	3.26	3.73	2.58	0.41	0.54	0.56	0.77	4.43	2.00	0.49	0.44	0.45
Tm	0.46	0.46	0.48	0.55	0.36	0.061	0.067	0.083	0.13	0.69	0.30	0.091	0.068	0.067
Yb	3.07	2.97	3.27	3.76	2.56	0.38	0.45	0.57	1.11	4.88	1.83	0.70	0.45	0.39
Lu	0.45	0.43	0.48	0.54	0.36	0.055	0.072	0.075	0.19	0.69	0.25	0.13	0.057	0.060
ΣREE	58.71	57.27	50.37	63.58	37.12	43.94	64.18	72.41	21.14	81.94	54.83	12.16	45.68	55.01
Trace elements (ppm)														
Sc	40.8	41.6	33.8	26.3	49.1	3.49	3.49	1.19	5.92	12.4	2.01	1.79	2.02	2.63
V	444	491	332	247	257	17.8	20.7	2.02	30.3	20.0	3.00	5.15	9.45	10.5
Cr	54.3	6.22	6.15	3.65	57.8	10.5	14.2	1.20	3.33	2.38	0.99	6.66	1.57	1.26
Co	46.8	45.0	31.1	20.0	44.9	3.24	3.98	0.34	1.32	2.91	0.30	0.83	1.61	1.63
Ni	26.4	4.94	4.52	4.20	54.6	6.91	13.8	0.35	5.95	1.40	0.36	2.70	0.93	0.51
Cu	4.58	5.41	4.95	30.0	35.0	2.49	6.64	2.10	2.44	3.01	3.77	4.42	10.2	2.49
Zn	78.3	58.2	35.5	21.3	36.4	21.4	28.0	32.9	5.42	12.4	46.3	7.83	33.4	36.7
Ga	15.1	19.6	12.8	17.5	12.5	17.6	16.1	19.9	10.4	11.8	25.7	11.0	16.8	18.4
Rb	5.54	0.50	1.32	0.17	6.52	59.2	5.01	54.4	3.44	1.00	127	1.48	25.4	22.1
Sr	173	142	103	255	172	344	234	244	145	51.8	40.0	196	223	249
Y	28.8	28.6	30.0	35.1	24.1	5.07	6.26	6.57	7.20	42.4	25.0	5.00	5.07	5.18
Zr	64.1	59.0	61.4	77.9	34.7	121	138	54.1	140	151	49.5	36.8	131	135
Nb	2.12	1.58	2.36	3.12	1.40	1.54	1.60	3.39	1.15	1.85	7.48	1.68	1.68	1.85
Ta	0.14	0.11	0.16	0.22	0.093	0.11	0.11	0.35	0.12	0.13	1.21	0.15	0.14	0.15
Cs	0.51	0.11	0.50	0.067	3.69	2.95	0.27	1.74	0.15	0.12	3.27	0.15	2.23	0.94
Ba	93.4	52.3	32.9	6.53	85.6	198	104	298	77.9	35.1	163	131	242	247
Hf	1.88	1.71	1.87	2.33	1.11	3.18	3.57	2.25	4.47	4.33	3.35	1.39	3.46	3.52
Pb	0.85	0.62	0.23	1.01	0.35	4.00	4.42	6.42	0.77	0.42	9.85	3.62	8.59	2.62
Th	0.61	0.55	0.48	0.65	0.30	2.61	3.55	4.38	2.95	1.29	3.71	0.091	3.21	3.35
U	0.34	0.30	0.52	0.54	0.41	0.79	0.95	1.43	0.44	0.45	2.74	0.16	0.79	0.78

Table 2. U–Pb zircon SIMS data for plagiogranite from the Yueyashan–Xichangjing ophiolite

Sample spot	U (ppm)	(ppm)	Th/U Th	f_{206}* (%)	$^{207}Pb/^{206}Pb$	±1σ (%)	$^{207}Pb/^{235}U$	±1σ (%)	$^{206}Pb/^{238}U$	±1σ (%)	$^{207}Pb–^{206}Pb$ Ma	±1σ	$^{207}Pb–^{235}U$ Ma	±1σ	$^{206}Pb–^{238}U$ Ma	±1σ
08YYS01	162	24	0.15	0.03	0.05763	1.21345	0.66269	1.93	0.08341	1.51	515.6	26.4	516.3	7.9	516.4	7.5
08YYS02	64	2	0.03	0.10	0.05606	1.98488	0.66807	2.49	0.08643	1.51	454.8	43.5	519.5	10.2	534.4	7.7
08YYS03	287	70	0.25	0.08	0.05756	0.99635	0.69455	1.80	0.08752	1.50	513.0	21.7	535.5	7.5	540.8	7.8
08YYS04	260	59	0.23	0.05	0.05886	1.36890	0.70725	2.04	0.08715	1.51	561.9	29.6	543.1	8.6	538.7	7.8
08YYS05	164	25	0.15	0.05	0.05801	1.59486	0.69966	2.19	0.08748	1.50	530.0	34.6	538.6	9.2	540.6	7.8
08YYS06	209	8	0.04	0.10	0.05781	1.16883	0.70028	1.90	0.08785	1.50	522.7	25.4	539.0	8.0	542.8	7.8
08YYS07	306	90	0.29	0.03	0.05799	1.17018	0.69089	1.91	0.08641	1.50	529.2	25.4	533.3	7.9	534.3	7.7
08YYS08	107	13	0.13	0.11	0.05957	2.25088	0.70512	2.72	0.08585	1.52	588.0	48.1	541.8	11.5	530.9	7.8
08YYS09	127	6	0.04	0.00	0.05689	1.40291	0.68212	2.05	0.08697	1.50	487.1	30.7	528.1	8.5	537.6	7.7
08YYS10	104	11	0.11	0.00	0.05894	1.81985	0.70619	2.36	0.08690	1.50	564.9	39.1	542.5	10.0	537.1	7.7
08YYS11	129	15	0.11	0.07	0.05770	1.51709	0.68263	2.13	0.08581	1.50	518.2	33.0	528.4	8.8	530.7	7.7
08YYS12	190	33	0.17	0.16	0.05842	1.31149	0.68923	1.99	0.08557	1.50	545.5	28.4	532.3	8.3	529.3	7.6
08YYS13	342	110	0.32	0.02	0.05798	0.86863	0.70808	1.73	0.08858	1.50	528.9	18.9	543.6	7.3	547.1	7.9
08YYS14	299	97	0.33	0.07	0.05724	0.97878	0.69102	1.80	0.08755	1.51	501.0	21.4	533.4	7.5	541.0	7.8
08YYS15	302	80	0.27	0.06	0.05721	1.18668	0.68938	1.91	0.08740	1.50	499.5	25.9	532.4	8.0	540.1	7.8
08YYS16	104	10	0.09	0.12	0.05653	2.13034	0.65757	2.61	0.08436	1.50	473.4	46.4	513.1	10.6	522.1	7.5
08YYS17	341	117	0.34	0.07	0.05721	0.91624	0.68526	1.76	0.08687	1.50	499.8	20.1	529.9	7.3	537.0	7.7
08YYS18	80	1	0.01	0.12	0.05654	2.04699	0.66373	2.54	0.08514	1.50	473.6	44.7	516.9	10.3	526.7	7.6
08YYS19	186	1	0.01	0.09	0.05726	1.27913	0.67361	1.98	0.08532	1.51	501.5	27.9	522.9	8.1	527.8	7.7
08YYS20	204	27	0.13	0.04	0.05799	1.12454	0.69400	1.88	0.08680	1.50	529.4	24.5	535.2	7.8	536.6	7.7

f_{206}* is the percentage of common ^{206}Pb in total ^{206}Pb

form a tight cluster on a Concordia diagram and yield a weighted mean ^{206}Pb–^{238}U age of 533 ± 1.7 Ma (95 % confidence level, MSWD = 6.7, n = 20; Fig. 12), which we consider to be the crystallization age of the plagiogranite. As an ophiolite component, plagiogranite is thought to have intruded at a late stage of magma crystallization (e.g. Floyd, Yaliniz & Goncuoglu, 1998). The above data suggest that the Yueyashan–Xichangjing ophiolitic ocean floor formed in early Cambrian time.

5. Discussion

5.a. Tectonic setting and age of the Yueyashan–Xichangjing ophiolite

In the past, the Yueyashan–Xichangjing ophiolite was considered to be derived from a typical N-MORB-type oceanic crust and mantle (Zuo *et al*. 1990*a,b*, 1991; Hsu *et al*. 1992; Liu & Wang, 1995; Zhou, Zhao & Li, 2000; Gong *et al*. 2003). However, new geochemical data of all the basaltic samples presented in this paper show spikes in large-ion lithophile fluid-mobile elements and negative anomalies in HFSEs (i.e. Zr, Hf, Nb, Ta; Fig. 10a,c,e), which are commonly attributed to an aqueous fluid component in the source region (Ellam & Hawkesworth, 1988; Brenan *et al*. 1995; Dhuime *et al*. 2007). Most rocks plot as N-MORB in petrogenetic-based discrimination diagrams (Pearce, 2008) (Fig. 9d). Notably in Figure 9c, some data points lie above the N-MORB–OIB line (Fig. 9c) and plot along a line towards the volcanic arc array, indicating an N-MORB mantle source and SSZ signature, and therefore suggest an SSZ-type ophiolite (Pearce *et al*. 1984; Stern & Bloomer, 1992; Pearce, 2008; Pearce & Robinson, 2010). We therefore interpret this ophiolite to reflect subduction of a main ocean, which was originally opened in Precambrian time by rifting and separation of the Huaniushan micro-continent from the Siberian margin (Fig. 13a,b).

The mafic and ultramafic rocks of the Yueyashan–Xichangjing ophiolite were originally considered to be intruded in middle Ordovician time (Anonymous, 1977). Later, Sm–Nd isotopic analyses of plagiogranites and mafic dykes yielded an isochron age of 468 ± 58 Ma (Zhou, Zhao & Li, 2000). In this study, we present a new weighted mean ^{206}Pb–^{238}U age of 533 ± 1.7 Ma (95 % confidence level, MSWD = 6.7, n = 20, Fig. 12) for a plagiogranite from the ophiolite, which we consider reflects the crystallization age; accordingly this suggests that the Yueyashan–Xichangjing ophiolite formed in early Cambrian time (Fig. 13b).

5.b. Emplacement of the Yueyashan–Xichangjing ophiolite

The tectonic polarity of Yueyashan–Xichangjing ophiolite is controversial. Some authors think that emplacement was caused by oceanic crust subduction beneath the Huaniushan micro-continental block to the south (Zuo *et al*. 1990*a*, 1991; Zuo, Liu & Liu,

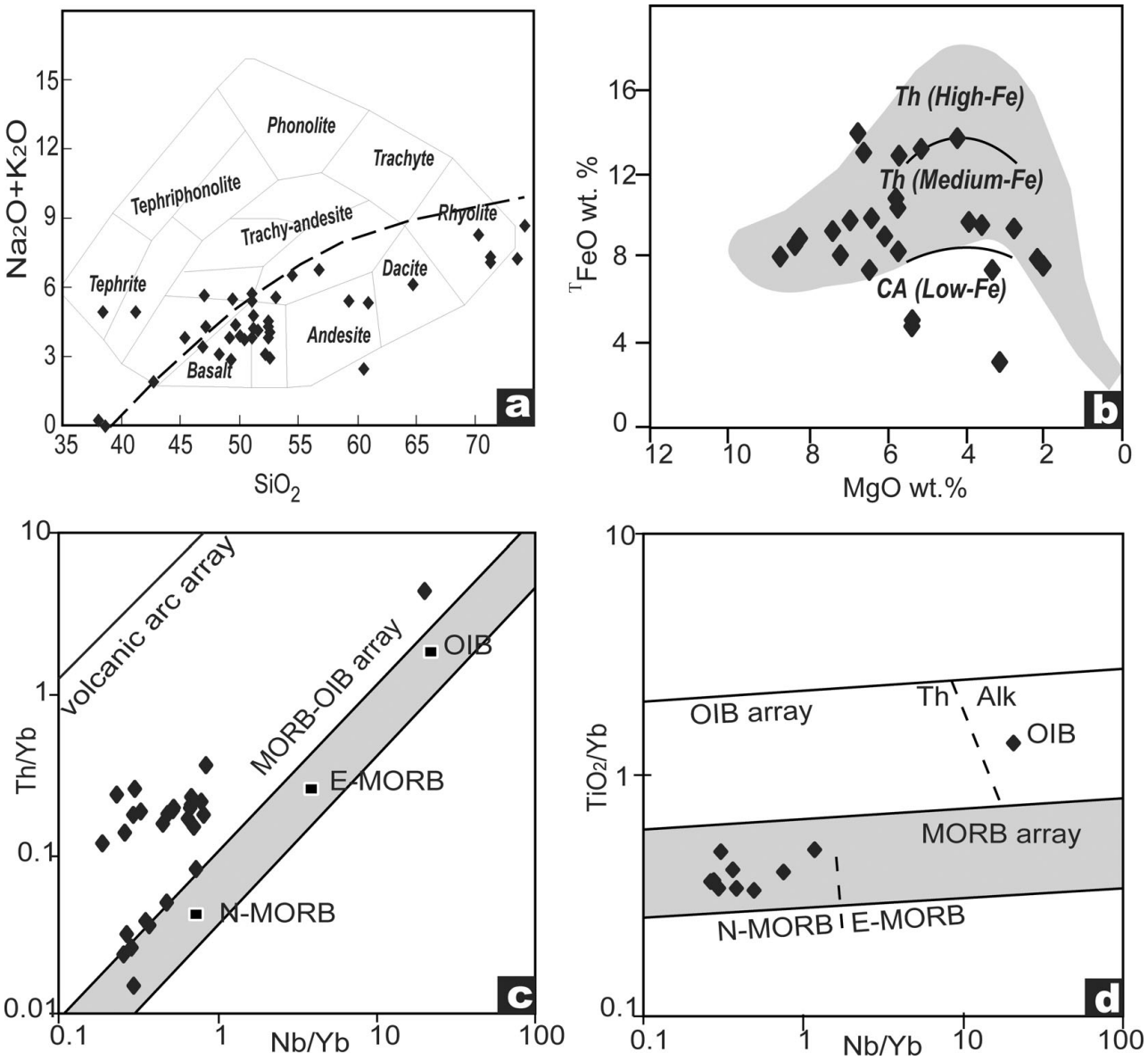

Figure 9. (a) $K_2O + Na_2O$ versus SiO_2 diagram (Le Maitre *et al*. 1989); the dashed line is the boundary between alkaline (above) and sub-alkaline (below) fields. (b) ^{T}FeO versus MgO diagram (Pearce & Robinson 2010); this diagram divides lavas into high, medium and low iron, where high- and medium-Fe can be treated as tholeiitic (Th) and low-Fe as calc-alkalic (CA). (c) Th/Yb versus Nb/Yb diagram (Pirajno *et al*. 2008). MORB – mid-ocean ridge basalt; OIB – ocean island basalt. (d) TiO_2/Yb versus Nb/Yb diagram (Pirajno *et al*. 2008). Th – tholeiitic series; Alk – alkalic series.

2003). Others infer that the Yueyashan–Xichangjing ophiolite was emplaced onto the northern margin of the Huaniushan block owing to subduction beneath the Mazongshan arc to the north (Liu & Wang, 1995; He *et al*. 2002, 2005). If the first idea were correct, the accretionary complex and arc-related intrusions should be to the south of the ophiolite. However, the second model is more likely, because as shown in Figure 2, the lithotectonic units from south to north are: the Huaniushan block (Unit I), a passive margin (Unit II), the incoherent Yueyashan–Xichangjing ophiolite (Unit III), the coherent sedimentary complex (Unit IV) and the Mazongshan island arc with arc-related intrusions (Unit V). Furthermore, the structural analysis of Unit IV shows that this sedimentary complex is dominantly characterized by folding and thrusting. Most thrusts dip NE and indicate top-to-the-SW translation (Figs 4, 6). Thus, the present data are more consistent with the idea that the emplacement of the Yueyashan–Xichangjing ophiolite was caused by oceanic crust subduction beneath the Mazongshan island arc to the north (Fig. 13c), followed by obduction of the ophiolite onto the northern margin of the Huaniushan block to the south.

Our data suggest that this event led to the main deformation phase in the Yueyashan–Xichangjing ophiolite belt, which is characterized by folding and thrusting with shortening in a NE–SW direction, perpendicular to the plate boundary (Figs 4, 5, 6). The emplacement of the Yueyashan–Xichangjing ophiolite was associated with a component of right-lateral, E–W, strike-slip faulting (Fig. 8); strain partitioning between

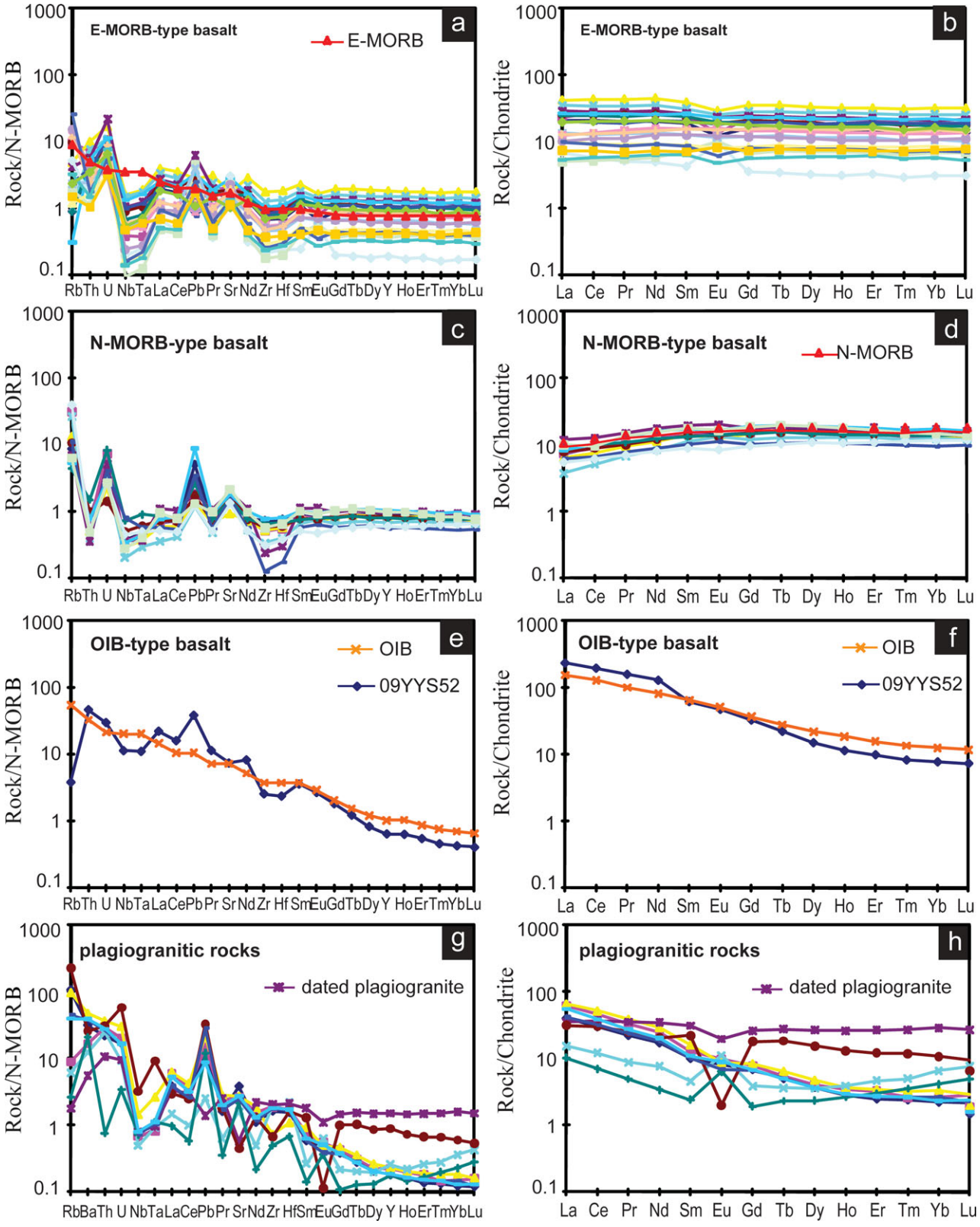

Figure 10. (Colour online) Chondrite-normalized REE patterns (b, d, f, h) and N-MORB normalized trace element spidergrams (a, c, e, g) of the Yueyashan–Xichangjing ophiolite (Sun & McDonough, 1989).

strike-slip and compressional motion is a well-known phenomenon in a transpressional setting (Cunningham, 2005, 2007).

The final emplacement of the Yueyashan–Xichangjing ophiolite can be considered to represent the end of subduction and the finalization of arc and micro-continent collision. The timing of this event is constrained by the youngest late Ordovician to early Silurian (Fig. 13d) age of Unit IV. Abundant gastropods, brachiopods, corals and trilobites in the lower part of Unit IV have been identified as middle to late Ordovician in age: *Maclurites* sp., *Lesueurilla* sp.,

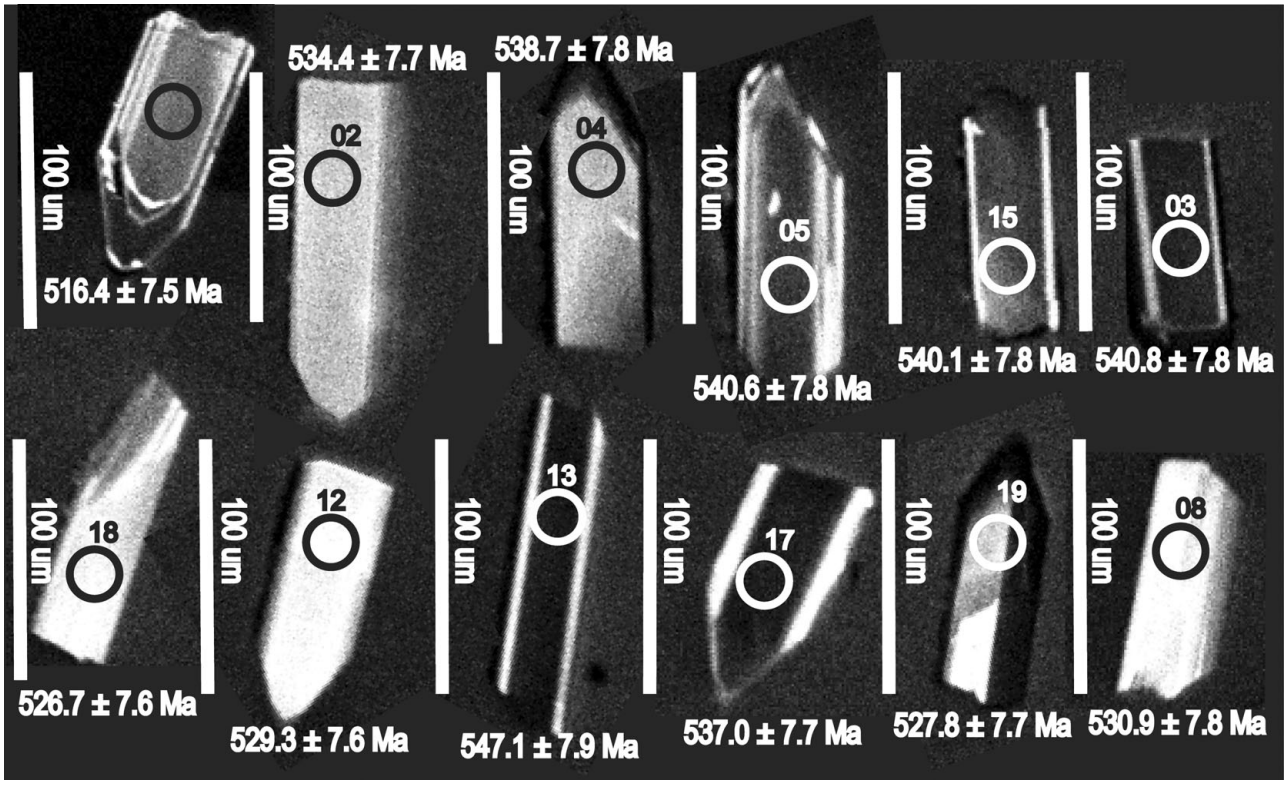

Figure 11. Representative cathodoluminescence images of zircons from the Yueyashan–Xichangjing ophiolite plagiogranite.

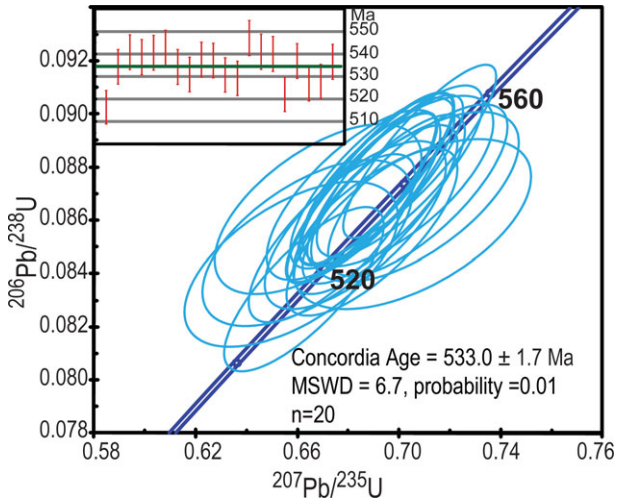

Figure 12. (Colour online) U–Pb Concordia diagram for zircons from a plagiogranite in the Yueyashan–Xichangjing ophiolite. Data-point error ellipses are 2σ. The weighted average plots of ^{206}Pb–^{238}U apparent ages are shown in the upper left corner box.

Heliolites sp., *Cyclospira bilobaria*, *Sphaerexochus* sp. and *Cerauninus* sp. (Anonymous, 1977, 1979). We consider that these fossil ages indicate that the Yueyashan–Xichangjing ophiolite was emplaced in late Ordovician to early Silurian time (Fig. 13d).

5.c. Tectonic evolution modal of the Yueyashan–Xichangjing ophiolite

Based on the above analysis of the structure, geochemistry and geochronology of the Yueyashan–Xichangjing ophiolite, we present a new tectonic history of the ophiolite illustrated in Figure 13.

5.c.1. Precambrian

At some time in the Precambrian the Gondwana supercontinent broke into the Siberia, Tarim–Dunhuang and some micro-continental blocks (e.g. Huaniushan) within the Palaeo-Asian Ocean, the subduction of which joined the Siberian block to the north with the Tarim–Dunhuang block to the south (Fig. 13a).

5.c.2. Early Cambrian

The northern margin of the Huaniushan micro-continental block has probably been a passive continental margin since Precambrian time. Sediments derived from the micro-continental block were deposited on the passive margin after early Cambrian time. N-dipping subduction of intra-oceanic lithosphere generated the Yueyashan–Xichangjing ophiolite at 533 ± 1.7 Ma, which was characterized by a SSZ geochemical signature (Zhou, Zhao & Li, 2000) (Fig. 13b). Oceanic sediments were scraped off the intra-oceanic subduction zone to form the accretionary complex at the same time.

5.c.3. Early to middle Ordovician

Sediments derived from the Huaniushan micro-continental block were deposited on the northern passive margin in early to middle Ordovician time. As

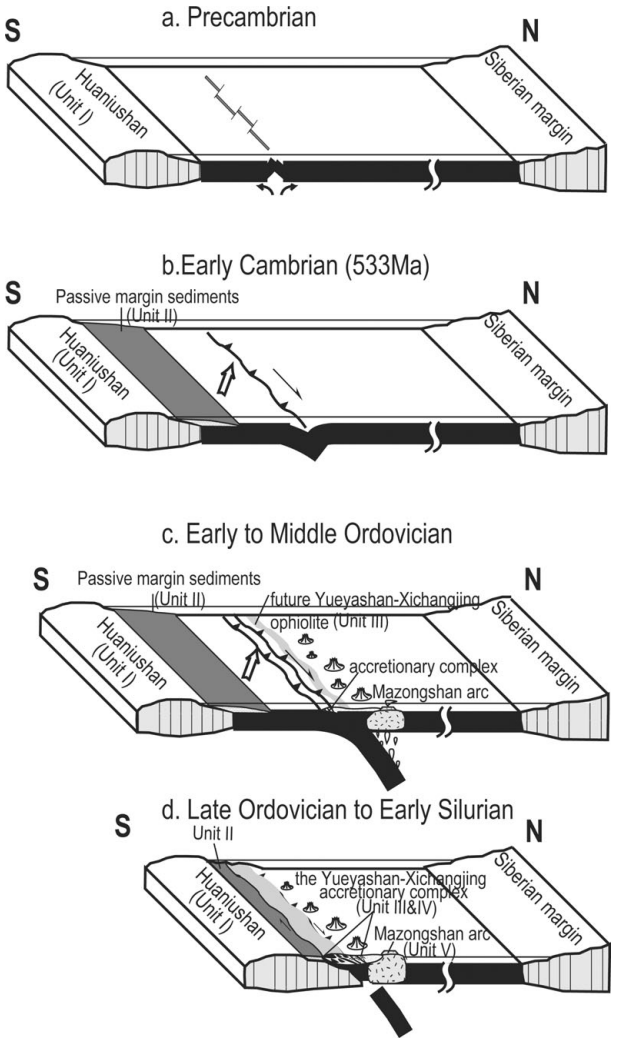

Figure 13. Schematic diagram showing the early Palaeozoic tectonic evolution of the Yueyashan–Xichangjing ophiolite in the Beishan area. (a) Precambrian; (b) early Cambrian; (c) early to middle Ordovician; (d) late Ordovician to early Silurian. See text for discussion.

subduction continued, an intra-oceanic arc (Mazongshan arc) was constructed above the subduction zone in early Ordovician time (Fig. 13c).

5.c.4. Late Ordovician to early Silurian

The Palaeo-Asian Ocean between the Huaniushan micro-continental block and the Mazongshan oceanic arc was probably consumed in late Ordovician to early Silurian time, and oceanic crust subduction continued beneath the Mazongshan arc to the north (Fig. 13d). This subduction and accretion caused the Yueyashan–Xichangjing ophiolite to be emplaced on the northern margin of the Huaniushan micro-continental block. Also, the Huaniushan micro-continental block and the Mazongshan arc were welded together as a composite block, which later took part in accretionary processes of the Altaids (see fig. 20 in Xiao *et al*. 2010*b*).

5.d. Significance

In the southern Altaids, early Palaeozoic orogenesis in the Beishan was characterized by Cambrian to early Silurian accretionary processes marked by the Yueyashan–Xichangjing ophiolite and associated rocks, which made up an early Palaeozoic accretionary complex (Zuo *et al*. 1990*a,b*, 1991; Zuo, Liu & Liu, 2003; Xiao *et al*. 2010*a,b*). The earliest subduction event was at 533 ± 1.7 Ma as recorded in the Yueyashan–Xichangjing ophiolite with its SSZ-type geochemistry. Combined with previously published Cambrian SSZ-type ophiolites (sphene Pb–Pb age of 523.2 ± 7.2 Ma (Kwon *et al*. 1989); SHRIMP zircon age 503 ± 7 Ma (Xiao *et al*. 2009)) in the southern Altaids, our data suggest that the Yueyashan–Xichangjing ophiolite records the earliest subduction event in the southern Altaids.

The Dunzhugur SSZ-type ophiolite in Eastern Sayan in the northern Altaids was dated at *c*. 1.0 Ga, which documents the earliest subduction event in the whole Central Asian Orogenic Belt (Khain *et al*. 2002, 2003). Younger subduction events in the Palaeozoic are recorded in surrounding areas (Cambrian: Dobretsov, Buslov & Vernikovsky, 2003; Dobretsov & Buslov, 2007; Rojas-Agramonte *et al*. 2011; Ordovician to late Carboniferous: Dobretsov, 2003; Rippington, Cunningham & England, 2008; Batkhishig, Noriyoshi & Greg, 2010). Therefore, the accretionary events in the northern Altaids lasted from *c*. 1.0 Ga to late Palaeozoic time. Our data together with published literature indicate that subduction events in the southern Altaids lasted from early Cambrian to Carboniferous–Permian time (Xiao *et al*. 2004*b*, 2008; Windley *et al*. 2007; Ao *et al*. 2010).

Clearly, some periods of accretion overlapped both in the northern and southern Palaeo-Asian Ocean. Therefore, the general southward, (present coordinates) single-subduction zone model for the whole Altaids (Şengör, Natal'in & Burtman, 1993; Şengör & Natal'in, 1996; Bazhenov *et al*. 2003; Collins *et al*. 2003; Abrajevitch *et al*. 2007; Levashova *et al*. 2007) can no longer explain the currently available data, and certainly requires considerable modification and update to account for the present well-documented evidence of multiple, subduction and accretion. In contrast, punctuated accretion and closure of multiple ocean basins provides a more viable and robust model for the accretionary processes of the Altaids. Yet, future work is required to further confirm the complicated multiple accretionary features of the Altaids.

Acknowledgements. We thank Q. L. Li, H. Li, X. D. Jin and X. Yan for their laboratory assistance, and Q. G. Mao for fruitful discussions. We appreciate the editor Phil Leat and Timothy Kusky, Brian Windley and Sanzhong Li for their constructive reviews. We gratefully acknowledge funds from the Chinese State 973 Programme (2007CB411307), the National 305 project (2011BAB06B04-1), the Innovative Programme of the Chinese Academy of Science (KZCX2-YW-Q04-08) and the National Natural Science Foundation of China (40725009, 40523003 and 40973036).

References

ABRAJEVITCH, A., VAN DER VOO, R., LEVASHOVA, N. M. & BAZHENOV, M. L. 2007. Paleomagnetic constraints on the paleogeography and oroclinal bending of the Devonian volcanic arc in Kazakhstan. *Tectonophysics* **441**, 67–84.

Anonymous. 1977. *Geological Map of the Wudaoming Region, China, 1:200,000*. The Geomechanics and Regional Geological Team of the Gansu Bureau of Geology (in Chinese).

Anonymous. 1979. *Geological Map of the Lujing Region, China, 1:200,000*. The Geomechanics and Regional Geological Team of the Gansu Bureau of Geology (in Chinese).

AO, S. J., XIAO, W. J., HAN, C. M., MAO, Q. G. & ZHANG, J. E. 2010. Geochronology and geochemistry of Early Permian mafic-ultramafic complexes in the Beishan area, Xinjiang, NW China: implications for late Paleozoic tectonic evolution of the southern Altaids. *Gondwana Research* **18**, 466–78.

BATKHISHIG, B., NORIYOSHI, T. & GREG, B. 2010. Magmatism of the Shuteen Complex and Carboniferous subduction of the Gurvansaikhan terrane, South Mongolia. *Journal of Asian Earth Sciences* **37**, 399–411.

BAZHENOV, M. L., COLLINS, A. Q., DEGTYAREV, K. E., LEVASHOVA, N. M., MIKOLAICHUK, A. V., PAVLOV, V. E. & VAN DER VOO, R. 2003. Paleozoic northward drift of the North Tien Shan (Central Asia) as revealed by Ordovician and Carboniferous paleomagnetism. *Tectonophysics* **366**, 113–41.

BRENAN, J. M., SHAW, H. F., PHINNEY, D. L. & RYERSON, F. J. 1994. Rutile-aqueous fluid partitioning of Nb, Ta, Hf, Zr, U and Th: implications for high field strength element depletions in island-arc basalts. *Earth and Planetary Science Letters* **128**, 327–39.

BRENAN, J. M., SHAW, H. F., RYERSON, F. J. & PHINNEY, D. L. 1995. Mineral-aqueous fluid partitioning of trace-elements at 900-degrees-C and 2.0 GPa – constraints on the trace-element chemistry of mantle and deep-crustal fluids. *Geochimica et Cosmochimica Acta* **59**, 3331–50.

BUCHAN, C., CUNNINGHAM, D., WINDLEY, B. F. & TOMURHUU, D. 2001. Structural and lithological characteristics of the Bayankhongor Ophiolite Zone, Central Mongolia. *Journal of the Geological Society, London* **158**, 445–60.

CARROLL, A. R., GRAHAM, S. A., HENDRIX, M. S., YING, D. & ZHOU, D. 1995. Late Paleozoic tectonic amalgamation of northwestern China: sedimentary record of the northern Tarim, northwestern Turpan, and southern Junggar Basins. *Geological Society of America Bulletin* **107**, 571–94.

CARROLL, A. R., YUNHAI, L., GRAHAM, S. A., XUCHANG, X., HENDRIX, M. S., JINCHI, C. & MCKNIGHT, C. L. 1990. Junggar basin, northwest China: trapped Late Paleozoic ocean. *Tectonophysics* **181**, 1–14.

CAWOOD, P. A., KRÖNER, A., COLLINS, W. J., KUSKY, T. M., MOONEY, W. D. & WINDLEY, B. F. 2009. Accretionary orogens through Earth history. In *Earth Accretionary Systems in Space and Time* (eds P. A. Cawood & A. Kröner), pp. 1–36. Geological Society of London, Special Publication no. 318.

COLEMAN, R.G. 1989. Continental growth of Northwest China. *Tectonics* **8**, 621–35.

COLLINS, A. Q., DEGTYAREV, K. E., LEVASHOVA, N. M., BAZHENOV, M. L. & VAN DER VOO, R. 2003. Early Paleozoic paleomagnetism of east Kazakhstan: implications for paleolatitudinal drift of tectonic elements within the Ural-Mongol belt. *Tectonophysics* **377**, 229–47.

CUNNINGHAM, D. 2005. Active intracontinental transpressional mountain building in the Mongolian Altai: defining a new class of orogen. *Earth and Planetary Science Letters* **240**, 436–44.

CUNNINGHAM, D. 2007. Structural and topographic characteristics of restraining bend mountain ranges of the Altai, Gobi Altai and easternmost Tien Shan. In *Tectonics of Strike-Slip Restraining and Releasing Bends* (eds W. D. Cunningham & P. Mann), pp. 219–37. Geological Society of London, Special Publication no. 290.

DHUIME, B., BOSCH, D., BODINIER, J. L., GARRIDO, C. J., BRUGUIER, O., HUSSAIN, S. S. & DAWOOD, H. 2007. Multistage evolution of the Jijal ultramafic-mafic complex (Kohistan, N Pakistan): implications for building the roots of island arcs. *Earth and Planetary Science Letters* **261**, 179–200.

DILEK, Y. & FURNES, H. 2011. Ophiolite genesis and global tectonics: geochemical and tectonic fingerprinting of ancient oceanic lithosphere. *Geological Society of America Bulletin* **123**, 387–411.

DOBRETSOV, N. L. 2003. Evolution of structures of the Urals, Kazakhstan, Tienshan and Altai-Sayan region within the Ural-Mongolian fold belt. *Russian Geology and Geophysics* **44**, 3–26.

DOBRETSOV, N. L. & BUSLOV, M. M. 2007. Late Cambrian-Ordovician tectonics and geodynamics of Central Asia. *Russian Geology and Geophysics* **48**, 71–82.

DOBRETSOV, N. L., BUSLOV, M. M. & VERNIKOVSKY, V. A. 2003. Neoproterozoic to Early Ordovician evolution of the Paleo-Asian Ocean: implications to the break-up of Rodinia. *Gondwana Research* **6**, 143–59.

ELLAM, R. M. & HAWKESWORTH, C. J. 1988. Elemental and isotopic variations in subduction related basalts – evidence for a three component model. *Contributions to Mineralogy and Petrology* **98**, 72–80.

FLOYD, P. A., YALINIZ, M. K. & GONCUOGLU, M. C. 1998. Geochemistry and petrogenesis of intrusive and extrusive ophiolitic plagiogranites, Central Anatolian Crystalline Complex, Turkey. *Lithos* **42**, 225–41.

GONG, Q. S., LIU, M. Q., LIANG, M. H. & LI, H. L. 2003. The tectonic facies and tectonic evolution of Beishan orogenic belt, Gansu. *Northwestern Geology* **1**, 11–17 (in Chinese with English abstract).

HE, S. P., REN, B. C., YAO, W. G. & FU, L. P. 2002. The division of tectonic units of Beishan area, Gansu-Inner Mongolia. *Northwestern Geology* **4**, 30–40 (in Chinese with English abstract).

HE, S. P., ZHOU, H. W., REN, B. C., YAO, W. G. & FU, L. P. 2005. Crustal evolution of Palaeozoic in Beishan area, Gansu and Inner Mongolia, China. *Northwestern Geology* **3**, 6–15 (in Chinese with English abstract).

HSU, K. J., YAO, Y. Y., LI, J. L. & WANG, Q. C. 1992. Geology of the Beishan Mountains and the tectonic evolution of Northwest China. *Eclogae Geologicae Helvetiae* **85**, 213–25.

HUANG, Z. B. & JIN, X. 2006. Geological characteristics and its setting for volcanic rocks of Baishan formation in Hongshishan area of Gansu Province. *Gansu Geology* **15**, 19–24 (in Chinese).

JAHN, B. M., WINDLEY, B., NATAL'IN, B. & DOBRETSOV, N. 2004. Phanerozoic continental growth in central Asia Preface. *Journal of Asian Earth Sciences* **23**, 599–603.

JAHN, B. M., WU, F. Y. & CHEN, B. 2000*a*. Granitoids of the Central Asian Orogenic Belt and continental growth in the Phanerozoic. *Transactions of the Royal Society of Edinburgh: Earth Sciences* **91**, 181–93.

JAHN, B. M., WU, F. Y. & CHEN, B. 2000*b*. Massive granitoid generation in Central Asia: Nd isotope evidence and implication for continental growth in the Phanerozoic. *Episodes* **23**, 82–92.

KHAIN, E. V., BIBIKOVA, E. V., KRÖNER, A., ZHURAVLEV, D. Z., SKLYAROV, E. V., FEDOTOVA, A. A. & KRAVCHENKO-BEREZHNOY, I. R. 2002. The most ancient ophiolite of the Central Asian fold belt: U-Pb and Pb-Pb zircon ages for the Dunzhugur Complex, Eastern Sayan, Siberia, and geodynamic implications. *Earth and Planetary Science Letters* **199**, 311–25.

KHAIN, E. V., BIBIKOVA, E. V., SALNIKOVA, E. B., KRÖNER, A., GIBSHER, A. S., DIDENKO, A. N., DEGTYAREV, K. E. & FEDOTOVA, A. A. 2003. The Palaeo-Asian ocean in the Neoproterozoic and early Palaeozoic: new geochronologic data and palaeotectonic reconstructions. *Precambrian Research* **122**, 329–58.

KWON, S. T., TILTON, G. R., COLEMAN, R. G. & FENG, Y. 1989. Isotopic studies bearing on the tectonics of the West Junggar region, Xinjiang, China. *Tectonics* **84**, 719–27.

LE MAITRE, R. W., BATEMAN, P., DUDEK, A., KELLER, J., LAMEYRE LE BAS, M. J., SABINE, P. A., SCHMID, R., SORENSEN, H., STRECKEISEN, A., WOOLLEY, A. R. & ZANETTIN, B. 1989. *A Classification of Igneous Rocks and a Glossary of Terms. Recommendations of the IGUS Subcommission on the Systematics of Igneous Rocks*. Oxford: Blackwell.

LEVASHOVA, N. M., MIKOLAICHUK, A. V., MCCAUSLAND, P. J. A., BAZHENOV, M. L. & VAN DER VOO, R. 2007. Devonian paleomagnetism of the North Tien Shan: implications for the middle-Late Paleozoic paleogeography of Eurasia. *Earth and Planetary Science Letters* **257**, 104–20.

LI, X.-H. 1997. Geochemistry of the Longsheng Ophiolite from the southern margin of Yangtze Craton, SE China. *Journal of Geochemistry* **31**, 323–37.

LI, Q.-L., LI, X.-H., LIU, Y., TANG, G. Q., YANG, J. H. & ZHU, W. G. 2010. Precise U-Pb and Pb-Pb dating of Phanerozoic baddeleyite by SIMS with oxygen flooding technique. *Journal of Analytical Atomic Spectrometry* **25**, 1107–13.

LI, X.-H., LIU, Y., LI, Q.-L., GUO, C.-H. & CHAMBERLAIN, K. R. 2009. Precise determination of Phanerozoic zircon Pb/Pb age by multicollector SIMS without external standardization. *Geochemistry, Geophysics, Geosystems* **10**, Q04010, doi:10.1029/2009GC002400, 21 pp.

LI, X.-H., LI, Z. X., WINGATE, M. T. D., CHUNG, S. L., LIU, Y., LIN, G. C. & LI, W. X. 2006. Geochemistry of the 755 Ma MundineWell dyke swarm, northwestern Australia: part of a Neoproterozoic mantle superplume beneath Rodinia? *Precambrian Research* **146**, 1–15.

LIU, X. Y. & WANG, Q. 1995. Tectonics and evolution of the Beishan orogenic belt, West China. *Geological Research* **10**, 151–65 (in Chinese with English abstract).

LUDWIG, K. R. 2001. *Users Manual for Isoplot/Ex rev. 2.49*. Berkeley Geochronology Centre Special Publication no. 1a, 56 pp.

MAO, J. W., PIRAJNO, F., ZHANG, Z. H., CHAI, F. M., WU, H., CHEN, S. P., CHENG, L. S., YANG, J. M. & ZHANG, C. Q. 2008. A review of the Cu-Ni sulphide deposits in the Chinese Tianshan and Altay orogens (Xinjiang Autonomous Region, NW China): principal characteristics and ore-forming processes. *Journal of Asian Earth Sciences* **32**, 184–203.

MAO, Q. G., XIAO, W. J., WINDLEY, B. F., HAN, C. M., QU, J. F., AO, S. J., ZHANG, J. E. & GUO, Q. Q. 2011. The Liuyuan complex in the Beishan, NW China: a Carboniferous–Permian forearc sliver in the southern Altaids. *Geological Magazine*. doi:10.1017/S0016756811000811.

MOORES, E. M. 1982. Origin and emplacement of ophiolites. *Reviews of Geophysics and Space Physics* **20**, 735–60.

PEARCE, J. A. 1983. The role of sub-continental lithosphere in magma genesis at destructive plate margins. In *Continental Basalts and Mantle Xenoliths* (eds C. J. Hawkesworth & M. J. Norry), pp. 230–49. Cheshire: Shiva Publishing.

PEARCE, J. A. 2008. Geochemical fingerprinting of oceanic basalts with applications to ophiolite classification and the search for Archean oceanic crust. *Lithos* **100**, 14–48.

PEARCE, J. A., HARRIS, J. & TINDLE, A. 1984. Trace element discrimination diagrams for the tectonic interpretation of granitic rocks. *Journal of Petrology* **25**, 956–83.

PEARCE, J. A. & ROBINSON, P. T. 2010. The Troodos ophiolitic complex probably formed in a subduction initiation, slab edge setting. *Gondwana Research* **18**, 60–81.

PIRAJNO, F., MAO, J. W., ZHANG, Z. C., ZHANG, Z. H. & CHAI, F. M. 2008. The association of mafic-ultramafic intrusions and A-type magmatism in the Tian Shan and Altay orogens, NW China: implications for geodynamic evolution and potential for the discovery of new ore deposits. *Journal of Asian Earth Sciences* **32**, 165–83.

RIPPINGTON, S., CUNNINGHAM, D. & ENGLAND, R. 2008. Structure and petrology of the Altan Uul Ophiolite: new evidence for a Late Carboniferous suture in the Gobi Altai, southern Mongolia. *Journal of the Geological Society, London* **165**, 711–23.

ROJAS-AGRAMONTE, Y., KRONER, A., DEMOUX, A., XIA, X., WANG, W., DONSKAYA, T., LIU, D. & SUN, M. 2011. Detrital and xenocrystic zircon ages from Neoproterozoic to Palaeozoic arc terranes of Mongolia: significance for the origin of crustal fragments in the Central Asian Orogenic Belt. *Gondwana Research* **19**, 751–63.

ŞENGÖR, A. M. C. & NATAL'IN, B. 1996. Paleotectonics of Asia: fragments of a synthesis. In *The Tectonic Evolution of Asia* (eds A. Yin & T. M. Harrison), pp. 486–641. Cambridge: Cambridge University Press.

ŞENGÖR, A. M. C., NATAL'IN, B.A. & BURTMAN, V. S. 1993. Evolution of the Altaid tectonic collage and Paleozoic crustal growth in Eurasia. *Nature* **364**, 299–307.

SHERVAIS, J. W. 1982. Ti-V plots and the petrogenesis of modern and ophiolitic lavas. *Earth and Planetary Science Letters* **59**, 101–18.

SONG, T. Z., WANG, J., LIN, H., YANG, X. F., ZHANG, L. & AN, S. W. 2008. The geological features of ophiolites of Xiaohuangshan in Beishan Area, Inner Mongolia. *Northwestern Geology* **3**, 55–63 (in Chinese with English abstract).

STACEY, J. S. & KRAMERS, J. D. 1975. Approximation of terrestrial lead isotope evolution by a two-stage model. *Earth and Planetary Science Letters* **26**, 207–21.

STERN, R. J. 2002. Subduction zones. *Reviews of Geophysics* **40**, 1012.

STERN, R. J. & BLOOMER, S. H. 1992. Subduction zone infancy: examples from the Eocene Izu-Bonin-Mariana and Jurassic California arcs. *Geological Society of America Bulletin* **104**, 1621–36.

SUN, S.-S. & MCDONOUGH, W. F. 1989. Chemical and isotopic systematics of oceanic basalts: implications for mantle composition and process. In *Magmatism in Ocean Basins* (eds A. D. Saunders & M. J. Norry), pp. 313–45. Geological Society of London, Special Publication no. 42.

WIEDENBECK, M., ALLÉ, P., CORFU, F., GRIFFIN, W., MEIER, M., OBERLI, F., QUADT, A. V., RODDICK, J. & SPIEGEL, W. 1995. Three natural zircon standards for U-Th-Pb, Lu-Hf, trace element and REE analyses. *Geostandards and Geoanalytical Research* **19**, 1–23.

WINDLEY, B. F., ALEXEIEV, D., XIAO, W. J., KRONER, A. & BADARCH, G. 2007. Tectonic models for accretion of the Central Asian Orogenic Belt. *Journal of the Geological Society, London* **164**, 31–47.

XIAO, W. J., HAN, C. M., YUAN, C., SUN, M., LIN, S. F., CHEN, H. L., LI, Z. L., LI, J. L. & SUN, S. 2008. Middle Cambrian to Permian subduction-related accretionary orogenesis of Northern Xinjiang, NW China: implications for the tectonic evolution of central Asia. *Journal of Asian Earth Sciences* **32**, 102–17.

XIAO, W. J., HUANG, B. C., HAN, C. M., SUN, S. & LI, J. L. 2010*a*. A review of the western part of the Altaids: a key to understanding the architecture of accretionary orogens. *Gondwana Research* **18**, 253–73.

XIAO, W. J., MAO, Q. G., WINDLEY, B. F., HAN, C. M., QU, J. F., ZHANG, J. E., AO, S. J., GUO, Q. Q., CLEVEN, N. R., LIN, S. F., SHAN, Y. H. & LI, J. L. 2010*b*. Paleozoic multiple accretionary and collisional processes of the Beishan orogenic collage. *American Journal of Science* **310**, 1553–94.

XIAO, W., WINDLEY, B. F., BADARCH, G., SUN, S., LI, J., QIN, K. & WANG, Z. 2004*a*. Palaeozoic accretionary and convergent tectonics of the southern Altaids: implications for the growth of Central Asia. *Journal of the Geological Society, London* **161**, 339–42.

XIAO, W. J., WINDLEY, B. F., YUAN, C., SUN, M., HAN, C. M., LIN, S. F., CHEN, H. L., YAN, Q. R., LIU, D. Y., QIN, K. Z., LI, J. L. & SUN, S. 2009. Paleozoic multiple subduction-accretion processes of the Southern Altaids. *American Journal of Science* **309**, 221–70.

XIAO, W. J., ZHANG, L. C., QIN, K. Z., SUN, S. & LI, J. L. 2004*b*. Paleozoic accretionary and collisional tectonics of the Eastern Tianshan (China): implications for the continental growth of Central Asia. *American Journal of Science* **304**, 370–95.

ZHANG, Y. Y. & GUO, Z. J. 2008. Accurate constraint on formation and emplacement age of Hongliuhe ophiolite, boundary region between Xinjiang and Gansu Provinces and its tectonic implications. *Acta Petrologica Sinica* **24**, 803–9 (in Chinese with English abstract).

ZHANG, Z. H., MAO, J. W., DU, A. D., PIRAJNO, F., WANG, Z. L., CHAI, F. M., ZHANG, Z. C. & YANG, J. M. 2008. Re-Os dating of two Cu-Ni sulfide deposits in northern Xinjiang, NW China and its geological significance. *Journal of Asian Earth Sciences* **32**, 204–17.

ZHOU, G. Q., ZHAO, J. X. & LI, X. H. 2000. Characteristics of the Yueyashan ophiolite from western Nei Mongol and its tectonic setting: geochemistry and Sm-Nd isotopic constraints. *Geochimica* **29**, 108–19 (in Chinese with English abstract).

ZUO, G. C., LIU, Y. K. & LIU, C. Y. 2003. Framework and evolution of the tectonic structure in Beishan area across Gansu Province, Xinjiang Autonomous region and Inner Mongolia Autonomous Region. *Acta Geologica Gansu* **12**, 1–15 (in Chinese with English abstract).

ZUO, G., ZHANG, S. L., HE, G. Q. & ZHANG, Y. 1990*a*. Early Paleozoic plate tectonics in Beishan area. *Scientia Geologica Sinica* **25**, 305–14 (in Chinese with English abstract).

ZUO, G., ZHANG, S., HE, G. & ZHANG, Y. 1991. Plate tectonic characteristics during the early paleozoic in Beishan near the Sino-Mongolian border region, China. *Tectonophysics* **188**, 385–92.

ZUO, G. C., ZHANG, S. L., WANG, X., JIN, S. Q., HE, G. Q., ZHANG, Y., LI, H. C. & BAI, W. C. 1990*b*. *Plate Tectonics and Metallogenic Regularities in Beishan Region.* Peking University Publishing House, pp. 144–88 (in Chinese with English abstract).

Appendix 1. Analytical procedures

SIMS U–Pb dating of zircon

Samples for U–Pb analysis were processed by conventional magnetic and density techniques to concentrate non-magnetic, heavy fractions. Zircon grains together with zircon standard 91500 were mounted in epoxy mounts, which were then polished in order to cut the crystals in half for analysis. All zircon grains were documented with transmitted and reflected light micrographs as well as cathodoluminescence images to reveal their internal structures, and the mount was vacuum-coated with high-purity gold prior to SIMS analysis. Measurements of U, Th and Pb were conducted using the Cameca IMS-1280 SIMS at the Institute of Geology and Geophysics, Chinese Academy of Sciences in Beijing. U–Th–Pb ratios and absolute abundances were determined relative to the zircon standard 91500 (Wiedenbeck *et al*. 1995), analyses of which were interspersed with those of unknown grains, using operating and data processing procedures similar to those described by Li *et al*. (2009). The mass resolution used to measure Pb/Pb and Pb/U isotopic ratios was 5400 during the analyses. A long-term uncertainty of 1.5 % (1 RSD) for $^{206}Pb/^{238}U$ measurements of the standard zircons was propagated by the unknowns (Li *et al*. 2010), despite the fact that the measured $^{206}Pb/^{238}U$ error in a specific session was generally around 1 % (1 RSD) or less. Measured compositions were corrected for common Pb using non-radiogenic ^{204}Pb. Corrections were sufficiently small to be insensitive to the choice of common Pb composition, and an average of present-day crustal composition (Stacey & Kramers, 1975) was used for the common Pb assuming that the common Pb is largely surface contamination introduced during sample preparation. Uncertainties of individual analyses in the data tables are reported at a 1σ level; mean ages for pooled U/Pb (and Pb/Pb) analyses are quoted with 95 % confidence intervals. Data reduction was carried out using the Isoplot/Ex v. 2.49 programs (Ludwig, 2001).

Whole-rock major and trace elements

All sample analyses were carried out at the Institute of Geology and Geophysics, Chinese Academy of Sciences in Beijing. Rock samples for whole-rock analyses were crushed and then pulverized in an agate mill. Whole-rock major elements were analysed by X-ray fluorescence (XRF) on fused glass beads, following the analytical procedures of Li *et al*. (2006). Analytical precision was between 1 % and 5 %. Trace elements were analysed using a PQ_2 Turbo ICP-MS, following the technique of Li (1997). About 50 mg of powder from each sample was dissolved in high-pressure Teflon bombs using a HF + HNO_3 mixture. An internal standard solution containing single element Rh was used for monitoring signal drift during ion counting. Within-run analytical precision for most elements was generally better than 2–5 %.